



Baroclinic instability with a simple model for vertical mixing

Matthew N. Crowe^{*} and John R. Taylor[†]

American Meteorological Society, Boston, Massachusetts

⁴ *Matthew N. Crowe, Department of Applied Mathematics and Theoretical Physics, University of

⁵ Cambridge, Centre for Mathematical Sciences, Wilberforce Road, Cambridge, CB3 0WA, UK

⁶ [†]Corresponding author address: Current affiliation: Department of Applied Mathematics and The-

⁷ oretical Physics, University of Cambridge, Centre for Mathematical Sciences, Wilberforce Road,

⁸ Cambridge, CB3 0WA, UK

⁹ E-mail: J.R.Taylor@damtp.cam.ac.uk

ABSTRACT

10 Here, we examine baroclinic instability in the presence of vertical mixing in
11 an idealized setting. Specifically, we use a simple model for vertical mixing
12 of momentum and buoyancy and expand the buoyancy and vorticity in a series
13 for small Rossby numbers. A flow in subinertial mixed layer (SML) balance
14 (Young (1994)) exhibits a normal mode linear instability which is studied here
15 using linear stability analysis and numerical simulations. The most unstable
16 modes grow by converting potential energy associated with the basic state
17 into kinetic energy of the growing perturbations. However, unlike the inviscid
18 Eady problem, the dominant energy balance is between the buoyancy flux and
19 the energy dissipated by vertical mixing. Vertical mixing reduces the growth
20 rate and changes the orientation of the most unstable modes with respect to the
21 front. By comparing with numerical simulations, we find that the predicted
22 scale of the most unstable mode matches the simulations for small Rossby
23 numbers while the growth rate and orientation agree for a broader range of
24 parameters. A stability analysis of a basic state in SML balance using the in-
25 viscid QG equations shows that the angle of the unstable modes is controlled
26 by the orientation of the SML flow, while stratification associated with an ad-
27 vection/diffusion balance controls the size of growing perturbations for small
28 Ekman numbers and/or large Rossby numbers. These results imply that baro-
29 clinic instability can be inhibited by small-scale turbulence when the Ekman
30 number is sufficiently large and might explain the lack of submesoscale ed-
31 dies in observations and numerical models of the ocean surface mixed layer
32 during summer.

33 **1. Introduction**

34 The ocean surface mixed layer plays a central role in the climate system by mediating transfers
35 of heat, carbon, and other important tracers between the atmosphere and deep ocean and influ-
36 encing the rate of primary production (Lorbacher et al. 2006; Sverdrup 1953). The mixed layer is
37 subject to intense small-scale turbulence driven by a wide variety of processes including convec-
38 tion, wind stress and breaking waves which lead to the nearly vertically uniform density field that
39 characterizes the mixed layer (Shay and Gregg 1986; Kato and Phillips 1969; Thorpe 2005).

40 The mixed layer also contains horizontal density gradients (e.g. Rudnick and Ferrari (1999)) in
41 the form of fronts on a wide range of horizontal scales (e.g. Callies and Ferrari (2013)). The avail-
42 able potential energy associated with the horizontal density gradients fuels mixed layer baroclinic
43 instability (or MLI) (Boccaletti et al. 2007; Fox-Kemper et al. 2008) which generates submesoscale
44 eddies while re-stratifying the mixed layer. Although MLI develops in a highly turbulent environ-
45 ment, most previous attempts at a linear stability analysis of MLI have neglected the influence of
46 small-scale turbulence. Our objective in this paper is to examine the influence of vertical mixing
47 on baroclinic instability.

48 Observations and numerical simulations have reported a strong seasonal cycle in submesoscale
49 activity (Capet et al. 2008; Mensa et al. 2013; Sasaki et al. 2014; Callies et al. 2015; Thompson
50 et al. 2016). Factors that could modulate submesoscale instabilities include the mixed layer depth,
51 horizontal density gradients, and turbulent mixing (e.g. Boccaletti et al. (2007); Bachman and
52 Taylor (2016); Callies and Ferrari (2018)). While the growth rate for MLI does not depend directly
53 on the mixed layer depth (Stone 1966; Fox-Kemper et al. 2008), the potential energy available for
54 release by MLI does (Callies et al. 2015). It remains unclear whether MLI is less energetic and
55 more difficult to detect in the summer, or whether it is arrested entirely. Here, we will show that

56 vertical mixing can arrest baroclinic instability in the limit of small Rossby numbers and strong
57 mixing. This result might help explain the lack of submesoscale activity in the summer.

58 Recently Callies et al. (2016) used a two layer Quasi-Geostrophic (QG) model to explore how
59 baroclinic mixed layer instability energizes submesoscale turbulence. Interestingly, their model
60 results are consistent with available observations, despite using the QG limit of small Rossby
61 number to describe structures with a Rossby number in the range of 0.1 – 1. This suggests that
62 QG dynamics may be useful to qualitatively describe submesoscale processes, although non-QG
63 dynamics are still needed to describe phenomena such as ageostrophic instabilities (e.g. symmetric
64 instability) and submesoscale frontogenesis (Shakespeare and Taylor 2013).

65 Young (1994) introduced the sub-inertial mixed layer (SML) model using an asymptotic expan-
66 sion in small Rossby number and a simple parameterization of turbulent mixing to consider the
67 effect of horizontal salinity and temperature gradients on shear and stratification in the mixed layer.
68 For a vertically-sheared flow in thermal wind balance, vertical mixing of momentum leads to an
69 ageostrophic secondary circulation. The secondary circulation acts to restratify the mixed layer, a
70 tendency which is balanced by vertical mixing to leading order. The vertically-sheared cross-front
71 flow associated with the secondary circulation and vertical mixing of temperature work together
72 to spread the front via shear dispersion (Young et al. 1982; Taylor 1953). Shear dispersion acting
73 on fronts was examined in Ferrari and Young (1997) and Crowe and Taylor (2018) for different
74 mixing parameterizations.

75 Young and Chen (1995) used the SML model to study baroclinic instability associated with
76 horizontal heat and salt gradients. For simplicity only cases of very strong and very weak mixing
77 were considered, with the strong mixing corresponding to a ‘slab’ mixed layer model with no
78 vertical variation and the weak mixing corresponding to a geostrophically balanced mixed layer.
79 They speculated that the classical Eady model of baroclinic instability (Eady 1949; Vallis 2006)

80 should be recovered in the limit of weak mixing. However, it was not possible to make this
81 connection explicitly since there is no background vertical stratification in the SML model and
82 the Richardson number is large (and hence stratification is strong) in the limit of small Rossby
83 numbers in the Eady model.

84 Crowe and Taylor (2018) considered the evolution of an isolated front subject to a depth-
85 dependent turbulent viscosity and diffusivity - a simple vertical mixing parameterization intended
86 to represent the effects of small-scale turbulence. The leading order momentum balance was found
87 to be the so-called ‘turbulent thermal wind’ (TTW) balance (Gula et al. 2014) between the Cori-
88 olis acceleration, the horizontal pressure gradient, and vertical mixing, with the resulting velocity
89 depending linearly on the horizontal buoyancy gradient. As in the SML model, vertically-sheared
90 cross-front flow leads to a re-stratification of the mixed layer, while shear dispersion leads to
91 spreading of the front.

92 Here, we take a different approach and use the vertical mixing scheme introduced by Young
93 (1994) to consider mixed layer instabilities in the presence of vertical mixing. Unlike Young
94 and Chen (1995) we use a single scalar, buoyancy, which simplifies the analysis for arbitrary
95 mixing intensity. We also include a background vertical stratification to allow direct comparison
96 with the Eady instability and we add horizontal viscous terms to examine the high wavenumber
97 cutoff. While similar to the SML model, our asymptotic approach differs in that the buoyancy
98 and momentum mixing timescales are assumed to be the same order, which leads to a different
99 parameter regime. The parameter regime we use is the same as that considered in Crowe and
100 Taylor (2018), although here the turbulent mixing is represented by relaxation towards the local
101 depth-averaged profile rather than diffusion.

102 In §2 we describe the governing equations and the asymptotic limit and discuss the differences
103 between our approach and the approach used by Young (1994); Young and Chen (1995). In §3 we

¹⁰⁴ give the asymptotic solution to the governing equations in terms of the background buoyancy field,
¹⁰⁵ b_0 , and horizontal streamfunction, ψ_0 . The governing equations for b_0 and ψ_0 are given in §4 and
¹⁰⁶ the instabilities of these equations are considered analytically in §5 and numerically in §6. In §7
¹⁰⁷ we use a quasi-geostrophic model to examine a mechanism that can control the fastest growing
¹⁰⁸ mode. Finally in §8 we discuss our results and the limitations of our model.

¹⁰⁹ 2. Governing Equations

¹¹⁰ We start with the 3D non-hydrostatic Boussinesq equations and consider a fluid bounded from
¹¹¹ above and below by flat, rigid boundaries in a coordinate system rotating about the vertical (z) axis.
¹¹² We invoke a linear equation of state and let the buoyancy, b , denote departures from a background
¹¹³ stratification with buoyancy frequency N . We non-dimensionalize the governing equations using
¹¹⁴ the horizontal length scale L , vertical length scale H , buoyancy scale Δb , horizontal velocity scale
¹¹⁵ $U = \Delta b H / (fL)$, vertical velocity scale $W = UH/L = \Delta b H^2 / (fL^2)$, pressure scale $P = fUL =$
¹¹⁶ $\Delta b H$, and timescale $T = L/U = fL^2 / (H\Delta b)$. This leads to the non-dimensional parameters defined
¹¹⁷ in Table 1.

¹¹⁸ We follow Young (1994) and parameterize vertical mixing by adding a forcing term to the RHS
¹¹⁹ of the momentum and buoyancy equations which acts to relax the velocity and buoyancy to the
¹²⁰ local depth-average. The rates of relaxation for buoyancy and velocity are μ_b and μ_u , respectively.
¹²¹ This parameterization is chosen largely for mathematical convenience though it is not conspicu-
¹²² ously less realistic than an eddy diffusivity parameterization. A similar analysis could be carried
¹²³ out with the vertical relaxation scheme replaced with a vertical viscosity and diffusivity. Although
¹²⁴ this complicates the analysis, qualitatively similar results can be obtained (see Appendix C).

With the choices described above, the non-dimensional governing equations are (Charney 1973; Young 1994; Crowe and Taylor 2018):

$$\text{Ro} \frac{Du}{Dt} - v = -\frac{\partial p}{\partial x} + \alpha (\bar{u} - u), \quad (1a)$$

$$\text{Ro} \frac{Dv}{Dt} + u = -\frac{\partial p}{\partial y} + \alpha (\bar{v} - v), \quad (1b)$$

$$\text{Ro} \epsilon^2 \frac{Dw}{Dt} = -\frac{\partial p}{\partial z} + b, \quad (1c)$$

$$\text{Ro} \frac{Db}{Dt} + \text{Bu} w = \frac{\alpha}{\text{Pr}_\alpha} (\bar{b} - b), \quad (1d)$$

$$\frac{\partial u}{\partial x} + \frac{\partial v}{\partial y} + \frac{\partial w}{\partial z} = 0, \quad (1e)$$

where the material derivative is

$$\frac{D}{Dt} = \frac{\partial}{\partial t} + \mathbf{u} \cdot \nabla, \quad (2)$$

and

$$\bar{\phi} = \int_{-1/2}^{1/2} \phi dz \quad (3)$$

denotes a depth average across the non-dimensional vertical domain $z \in [-1/2, 1/2]$. Note that we might expect the background stratification represented by Bu to be affected by vertical mixing. We instead assume that this stratification is maintained by a process that is not represented here and occurs on a different timescale to the mixing, such as symmetric instability or surface heating, so that the background stratification can be imposed as a constant. Note that a stable stratification will develop in response to mixing of momentum even if Bu = 0. Imposing an additional background stratification is mathematically convenient as it allows for a straightforward comparison with the Eady model in the limit of no vertical mixing.

Our approach differs from Young (1994) where it was assumed that the ratio of the buoyancy mixing timescale to the advection timescale was small compared to one, but large compared to the

¹³⁹ Rossby number, such that

$$\frac{1/\mu_b}{T} = \frac{\text{Ro} \Pr_\alpha}{\alpha} \gg \text{Ro}. \quad (4)$$

¹⁴⁰ Since no assumptions are made about the size of α , this results in the requirement that \Pr_α is
¹⁴¹ large unless α is small. Motivated by simulations and experiments of turbulent mixing in weakly
¹⁴² stratified flows, we instead assume that $\Pr_\alpha = O(1)$ (e.g. Schumann and Gerz (1995); Venayag-
¹⁴³ amoorthy and Stretch (2010)). This choice of \Pr_α allows us to consider the case where the mixing
¹⁴⁴ rates are similar for any value of α , although we are unable to solve the resulting equations to the
¹⁴⁵ same order in Ro as Young (1994).

¹⁴⁶ Before proceeding with the analysis, it is useful to relate our nondimensional parameters to
¹⁴⁷ physical quantities. We can relate the relaxation (mixing) rates, μ_u and μ_b , to a turbulent eddy
¹⁴⁸ turnover time by defining a characteristic turbulent velocity scale, u_* , and a characteristic length
¹⁴⁹ scale, l . The parameterized mixing rates, μ_u and μ_b , then scale with

$$\mu_u, \mu_b \sim \frac{u_*}{l}. \quad (5)$$

¹⁵⁰ Therefore, the ratio of the mixing rate to the Coriolis frequency is

$$\alpha \sim \frac{u_*}{lf}. \quad (6)$$

¹⁵¹ For wind-driven turbulence, the friction velocity provides a characteristic velocity scale such
¹⁵² that $u_* = \sqrt{\tau_w/\rho_0}$, where τ_w is the magnitude of the wind stress. In this case the turbulent length
¹⁵³ scale, l , characterizing the largest turbulent eddies would be the smaller of the mixed layer depth
¹⁵⁴ or the Ekman layer depth. On the other hand for convection an appropriate characteristic velocity
¹⁵⁵ scale is instead $u_* = w_* = (B_0 l)^{1/3}$ where B_0 is the surface buoyancy flux and l is the mixed layer
¹⁵⁶ (or convective layer) depth. Note that the relaxation ratio can be related to the Ekman number,

¹⁵⁷ $E = v/(fl^2)$, by invoking a mixing length argument where the turbulent viscosity, $v \sim u_*l$. Hence

$$\alpha \sim \frac{u_*}{lf} \sim \frac{v}{fl^2} \sim E. \quad (7)$$

¹⁵⁸ We can estimate some of the important parameters including the aspect ratio, Rossby number,
¹⁵⁹ and relaxation ratio from reported observations of fronts. We have selected three examples using
¹⁶⁰ observations reported in Mahadevan et al. (2012); Thompson et al. (2016); Thomas et al. (2013)
¹⁶¹ which correspond to weak, moderate, and strong horizontal density gradients, respectively. Note
¹⁶² that the values chosen from Mahadevan et al. (2012) correspond to the north/south density gradient
¹⁶³ characterizing the North Atlantic as observed during the North Atlantic Bloom Experiment, rather
¹⁶⁴ than individual fronts. The estimated parameter values are given in Table 2. Note also that the
¹⁶⁵ values are roughly representative of the observations, but the structure of the fronts are complicated
¹⁶⁶ and cannot be fully represented with a simple set of parameters. Nevertheless, the relatively weak
¹⁶⁷ north/south density gradient observed during the North Atlantic Bloom experiment (Mahadevan
¹⁶⁸ et al. 2012) and simulated by Mahadevan et al. (2012) and Taylor (2016) and the fronts reported
¹⁶⁹ in Thompson et al. (2016) have relatively small Rossby numbers using our definition. As we will
¹⁷⁰ show using comparisons with numerical simulations, aspects of our asymptotic theory are valid at
¹⁷¹ these Rossby numbers. In contrast, the Rossby number associated with the Gulf Stream front is
¹⁷² quite large and outside of the range of validity of our asymptotic theory. We note that it is possible
¹⁷³ to have $\alpha = O(1)$ for both strong and weak fronts and the aspect ratio, ϵ , is generally small for
¹⁷⁴ open ocean fronts.

¹⁷⁵ Note that our definition of Rossby number uses a length scale characteristic of the horizontal
¹⁷⁶ density gradient and not necessarily the resulting eddies. As a result, the Rossby number as defined
¹⁷⁷ here can be quite small in practice. If we instead define a Rossby number, Ro_s , using the length-
¹⁷⁸ scale of a baroclinic eddy, we have $Ro_s = K Ro$ for nondimensional wavenumber K . In the analysis

179 that follows, we will show that K can be on the order of 100, and hence $\text{Ro}_s = O(1)$ as typical of
180 a submesoscale eddy. Therefore, even though the values of Ro used in our theory and simulations
181 will be very small, our results are applicable to the formation of submesoscale structures where
182 $\text{Ro}_s \sim 1$.

183 3. Asymptotic Solution

184 In this section we will solve Eqns. (1a-1e) using an asymptotic method valid for small Rossby
185 numbers. We begin by assuming that the aspect ratio is small and expand all variables in powers
186 of Ro , e.g. $b = b_0 + \text{Ro}b_1 + \text{Ro}^2b_2 + \dots$. We impose no conditions on the relaxation rate, α , and
187 allow it to appear at leading order. We also assume that the stratification is weak with $\text{Bu} = O(\text{Ro})$,
188 hence we write $\text{Bu} = \text{Ro}\mathcal{N}^2$ where

$$189 \quad \mathcal{N}^2 = N^2 H / \Delta b, \quad (8)$$

190 is the ratio of the vertical buoyancy difference ($N^2 H$) to the horizontal buoyancy difference (Δb).
191 Here, for the purposes of the asymptotic equations we will assume that $\mathcal{N}^2 = O(1)$, although the
result will be valid if $\mathcal{N}^2 \ll 1$. The time derivative is expanded into fast and slow timescales:

$$192 \quad \frac{\partial}{\partial t} \rightarrow \frac{\partial}{\partial t} + \frac{1}{\text{Ro}} \frac{\partial}{\partial \tau}, \quad (9)$$

193 for fast transient timescale, $\tau = t/\text{Ro}$. The fast timescale, τ , represents the transient evolution
from a general initial condition. In order to simplify the analysis we assume that all transients
194 have decayed and hence neglect the τ derivatives. For completeness, the full solution including
195 the transients is given in Appendix A.

196 a. Order 1 Equations

197 We now consider separately the $O(1)$ and $O(\text{Ro})$ terms in the governing equations. With the
198 assumption that $\text{Bu} = O(\text{Ro})$, the only term in the buoyancy equation that contributes to $O(1)$ is

¹⁹⁹ the parameterized vertical mixing term. Hence, the $O(1)$ buoyancy balance is

$$\frac{\alpha}{\text{Pr}_\alpha} b'_0 = 0, \quad (10)$$

²⁰⁰ where $(\cdot)'$ denotes a departure from the local depth-average. Eq. 10 implies that b_0 is independent
²⁰¹ of depth. This is consistent with the limit of strong mixing leading to a well-mixed layer as also
²⁰² found by Young (1994).

²⁰³ Similarly, the leading order balance in the momentum equations is

$$-v_0 = -\frac{\partial p_0}{\partial x} - \alpha u'_0, \quad (11a)$$

$$u_0 = -\frac{\partial p_0}{\partial y} - \alpha v'_0, \quad (11b)$$

$$0 = -\frac{\partial p_0}{\partial z} + b_0, \quad (11c)$$

$$0 = \frac{\partial u_0}{\partial x} + \frac{\partial v_0}{\partial y} + \frac{\partial w_0}{\partial z}. \quad (11d)$$

²⁰⁴ Eq. 11c can be integrated to give $p_0 = z b_0 + \bar{p}_0$, and the depth-averaged horizontal momentum
²⁰⁵ equations and mass conservation equation reduce to geostrophic balance for the depth-averaged
²⁰⁶ flow:

$$-\bar{v}_0 = -\frac{\partial \bar{p}_0}{\partial x}, \quad (12a)$$

$$\bar{u}_0 = -\frac{\partial \bar{p}_0}{\partial y}, \quad (12b)$$

$$0 = \frac{\partial \bar{u}_0}{\partial x} + \frac{\partial \bar{v}_0}{\partial y}. \quad (12c)$$

²⁰⁷ Subtracting the depth-averaged horizontal momentum equations from equations 11 gives evolution
²⁰⁸ equations for the horizontal velocity perturbations and vertical velocity

$$\alpha u'_0 - v'_0 = -z \frac{\partial b_0}{\partial x}, \quad (13a)$$

$$\alpha v'_0 + u'_0 = -z \frac{\partial b_0}{\partial y}, \quad (13b)$$

$$0 = \frac{\partial u'_0}{\partial x} + \frac{\partial v'_0}{\partial y} + \frac{\partial w_0}{\partial z}. \quad (13c)$$

²⁰⁹ Equations 13 can be combined to give

$$\mathbf{u}'_{H0} = \gamma[-\alpha \nabla_H b_0 + \mathbf{k} \times \nabla_H b_0] z, \quad (14)$$

²¹⁰ and

$$w_0 = \frac{\alpha \gamma (4z^2 - 1)}{8} \nabla_H^2 b_0, \quad (15)$$

²¹¹ where $\gamma = 1/(1 + \alpha^2)$. From the depth-averaged mass conservation equation we can write $\bar{\mathbf{u}}_{H0} =$
²¹² $-\nabla \times (\psi_0 \mathbf{k})$ for streamfunction ψ_0 . From equations 12a and 12b we note that $\bar{p}_0 = \psi_0$. Hence

$$\mathbf{u}_{H0} = -\nabla \times (\psi_0 \mathbf{k}) + \gamma[-\alpha \nabla_H b_0 + \mathbf{k} \times \nabla_H b_0] z. \quad (16)$$

²¹³ As noted in Young (1994), the horizontal velocity has a non-zero vertical shear at leading order,
²¹⁴ unlike the buoyancy which is well-mixed at leading order. In the case of $\alpha = 0$, the equation for
²¹⁵ \mathbf{u}_{H0} reduces to thermal wind balance. For nonzero α , vertical mixing acts to couple the cross-
²¹⁶ front and along-front flows, leading to a flow with a component in the direction of the buoyancy
²¹⁷ gradient. For $\alpha < 1$ stronger mixing results in a stronger cross-front shear, while the cross-front
²¹⁸ shear weakens with stronger mixing for $\alpha > 1$.

²¹⁹ b. Order Ro Equations

²²⁰ We now consider the $O(\text{Ro})$ terms in the buoyancy conservation equation. The advection of b_0
²²¹ by the leading order velocity contributes to $O(\text{Ro})$. Since $b_0 = b_0(x, y, t)$, the $O(\text{Ro})$ buoyancy
²²² equation is

$$\frac{\partial b_0}{\partial t} + \mathbf{u}_{H0} \cdot \nabla_H b_0 + \mathcal{N}^2 w_0 = -\frac{\alpha}{\text{Pr}_\alpha} b'_1. \quad (17)$$

²²³ Subtracting the depth average gives

$$\frac{\alpha}{\text{Pr}_\alpha} b'_1 = -\mathbf{u}'_{H0} \cdot \nabla_H b_0 - \mathcal{N}^2 w'_0, \quad (18)$$

224 which describes a balance between advection by the cross-front flow and vertical mixing. Hence
225 the solution for b'_1 is

$$b'_1 = \text{Pr}_\alpha \gamma \left[z |\nabla_H b_0|^2 - \mathcal{N}^2 \frac{12z^2 - 1}{24} \nabla_H^2 b_0 \right]. \quad (19)$$

226 Solving for \bar{b}_1 requires the $O(\text{Ro}^2)$ buoyancy equation. Note that even with $\mathcal{N} = 0$, there is a stable
227 vertical stratification at this order, consistent with the finding from Tandon and Garrett (1994) that
228 the vertical buoyancy gradient is proportional to the horizontal buoyancy gradient squared.

229 4. Evolution of the Background Fields

230 In order to determine the time dependence of the system on the slow timescale, t , we need
231 to determine governing equations for the depth independent functions b_0 and ψ_0 . These can be
232 obtained by depth averaging the buoyancy and vertical vorticity equations. The vertical vorticity
233 equation is

$$\text{Ro} \left(\frac{\partial \zeta}{\partial t} + \mathbf{u} \cdot \nabla \zeta - \boldsymbol{\omega} \cdot \nabla w \right) + \nabla_H \cdot \mathbf{u}_H = \alpha (\bar{\zeta} - \zeta), \quad (20)$$

234 for vertical vorticity $\zeta = \boldsymbol{\omega} \cdot \mathbf{k}$, which can be depth-averaged to give

$$\frac{\partial \bar{\zeta}}{\partial t} + \nabla_H \cdot [\overline{\mathbf{u}_H \zeta} - \overline{\boldsymbol{\omega}_H w}] = 0, \quad (21)$$

235 or using depth-averaged and perturbation quantities,

$$\frac{\partial \bar{\zeta}}{\partial t} + \nabla_H \cdot [\overline{\mathbf{u}_H} \bar{\zeta} - \overline{\boldsymbol{\omega}_H} \bar{w} + \overline{\mathbf{u}'_H} \zeta' - \overline{\boldsymbol{\omega}'_H w'}] = 0. \quad (22)$$

236 Similarly, the depth-averaged buoyancy equation is

$$\frac{\partial \bar{b}}{\partial t} + \overline{\mathbf{u}_H} \cdot \nabla_H \bar{b} + \nabla_H \cdot [\overline{\mathbf{u}'_H} \bar{b'}] + \mathcal{N}^2 \bar{w} = 0. \quad (23)$$

237 We now use the leading order solutions for the velocity and buoyancy fields (ψ_0 and b_0) to write
238 the depth-averaged equations in terms of these fields.

²³⁹ *a. Buoyancy*

²⁴⁰ Substituting the expansions in Rossby number up to $O(\text{Ro})$ into Eq. 23 gives

$$\frac{\partial b_0}{\partial t} + \bar{\mathbf{u}}_{H0} \cdot \nabla_H b_0 + \mathcal{N}^2 \bar{w}_0 + \text{Ro} \left[\frac{\partial \bar{b}_1}{\partial t} + \bar{\mathbf{u}}_{H1} \cdot \nabla_H b_0 + \bar{\mathbf{u}}_{H0} \cdot \nabla_H \bar{b}_1 + \mathcal{N}^2 \bar{w}_1 + \nabla_H \cdot [\bar{\mathbf{u}}'_{H0} \bar{b}'_1] \right] = 0. \quad (24)$$

²⁴¹ Using the definition of ψ_0 , we can write $\bar{\mathbf{u}}_{H0} \cdot \nabla_H b_0 = J(\psi_0, b_0)$, where J is the Jacobian operator:

$$J(f, g) = \frac{\partial f}{\partial x} \frac{\partial g}{\partial y} - \frac{\partial f}{\partial y} \frac{\partial g}{\partial x}. \quad (25)$$

²⁴² We can also write the flux term as

$$\bar{\mathbf{u}}'_{H0} \bar{b}'_1 = \frac{\text{Pr}_\alpha \gamma^2}{12} (-\alpha \nabla_H b_0 + \mathbf{k} \times \nabla_H b_0) |\nabla_H b_0|^2, \quad (26)$$

²⁴³ and hence Eq. 24 can be written as

$$\begin{aligned} \frac{\partial b_0}{\partial t} + J(\psi_0, b_0) + \mathcal{N}^2 \bar{w}_0 + \text{Ro} \left[\frac{\partial \bar{b}_1}{\partial t} + \bar{\mathbf{u}}_{H1} \cdot \nabla_H b_0 + \bar{\mathbf{u}}_{H0} \cdot \nabla_H \bar{b}_1 + \mathcal{N}^2 \bar{w}_1 \right] \\ = \frac{\text{Ro} \text{Pr}_\alpha \gamma^2}{12} \nabla_H \cdot [(\alpha \nabla_H b_0 - \mathbf{k} \times \nabla_H b_0) |\nabla_H b_0|^2]. \end{aligned} \quad (27)$$

²⁴⁴ The limit considered by Young (1994) uses $\text{Pr}_\alpha = \mathcal{P}/\sqrt{\text{Ro}}$ with $\mathcal{P} = O(1)$. For $\text{Ro} \ll 1$ this
²⁴⁵ corresponds to momentum relaxation that is much faster than the buoyancy relaxation. With this
²⁴⁶ choice, and in the absence of background stratification ($N^2 = 0$), the buoyancy evolution equation
²⁴⁷ to order $O(\sqrt{\text{Ro}})$ can be written

$$\frac{\partial b_0}{\partial t} + J(\psi_0, b_0) = \frac{\sqrt{\text{Ro}} \mathcal{P} \gamma^2}{12} \nabla_H \cdot [(\alpha \nabla_H b_0 - \mathbf{k} \times \nabla_H b_0) |\nabla_H b_0|^2]. \quad (28)$$

²⁴⁸ This result was obtained by Young (1994). The first term in brackets on the right hand side of Eq.
²⁴⁹ 28 is a down-gradient buoyancy flux. The second term is a ‘skew’ flux directed perpendicular to
²⁵⁰ the buoyancy gradient. The role of the skew flux will be discussed in more detail in §4c.

²⁵¹ Here, we take a different approach from Young (1994) and assume that $\text{Pr}_\alpha = O(1)$ while re-
²⁵² taining a non-zero background stratification. The $O(1)$ terms in Eq. 27 are then

$$\frac{\partial b_0}{\partial t} + J(\psi_0, b_0) = \frac{\alpha \gamma \mathcal{N}^2}{12} \nabla_H^2 b_0, \quad (29)$$

where we have used $\bar{w}_0 = -\alpha\gamma(\nabla_H^2 b_0)/12$. With this form for w_0 , vertical advection acting on the background stratification ($\mathcal{N}^2 w_0$ in Eq. 27) acts like horizontal diffusion on the leading order buoyancy.

Crowe and Taylor (2018, 2019) studied the evolution of a front in turbulent thermal wind balance. A simple form of this problem can be obtained by considering a two-dimensional front with no y dependence and $\mathcal{N}^2 = 0$. With these assumptions, Eq. 27 reduces to

$$\frac{\partial b_0}{\partial t} = \frac{\text{Ro}\text{Pr}_\alpha\gamma^2\alpha}{12} \frac{\partial}{\partial x} \left(\frac{\partial b_0}{\partial x} \right)^3, \quad (30)$$

as \bar{b}_1 and \bar{u}_{H1} can be assumed to be zero by symmetry. This equation describes frontal spreading on the timescale $T = \text{Rot}$ and can be solved with a similarity solution as in Crowe and Taylor (2018).

b. Vorticity

We can formulate a closed system of two equations for the leading order buoyancy, b_0 , and the leading order streamfunction, ψ_0 , using conservation of vorticity. The leading order vorticity equation is

$$\frac{\partial \bar{\zeta}_0}{\partial t} + \nabla_H \cdot [\bar{\mathbf{u}}_{H0} \bar{\zeta}_0 - \bar{\omega}_{H0} \bar{w}_0 + \overline{u'_{H0} \zeta'_0} - \overline{\omega'_{H0} w'_0}] = 0, \quad (31)$$

where each term can now be written in terms of b_0 and ψ_0 . The leading order vertical vorticity is

$$\zeta_0 = \frac{\partial v_0}{\partial x} - \frac{\partial u_0}{\partial y} = \nabla_H^2 \psi_0 + \gamma z \nabla_H^2 b_0. \quad (32)$$

Since b_0 is independent of z , and since z is anti-symmetric about the mid-plane ($z = 0$), the final term does not contribute to the depth-average, which leaves $\bar{\zeta}_0 = \nabla_H^2 \psi_0$. Advection of vorticity by the depth-averaged horizontal velocity can be written as

$$\nabla_H \cdot [\bar{\mathbf{u}}_{H0} \bar{\zeta}_0] = \nabla_H \cdot [\bar{\mathbf{u}}_{H0} \nabla_H^2 \psi_0] = J(\psi_0, \nabla_H^2 \psi_0). \quad (33)$$

²⁷⁰ The horizontal vorticity is given by

$$\boldsymbol{\omega}_{H0} = \begin{pmatrix} \frac{\partial w_0}{\partial y} - \frac{\partial v_0}{\partial z} \\ \frac{\partial u_0}{\partial z} - \frac{\partial w_0}{\partial x} \end{pmatrix}, \quad (34)$$

²⁷¹ and its depth-average is

$$\overline{\boldsymbol{\omega}}_{H0} = \begin{pmatrix} \frac{\partial \bar{w}_0}{\partial y} - \Delta v_0 \\ \Delta u_0 - \frac{\partial \bar{w}_0}{\partial x} \end{pmatrix}, \quad (35)$$

²⁷² where Δu_0 and Δv_0 are the change in horizontal velocity between the top and bottom boundaries.

²⁷³ The second flux term is

$$\nabla_H \cdot [\overline{\boldsymbol{\omega}}_{H0} \bar{w}_0] = \nabla_H \cdot \left[\frac{1}{2} \begin{pmatrix} \frac{\partial \bar{w}_0^2}{\partial y} \\ -\frac{\partial \bar{w}_0^2}{\partial x} \end{pmatrix} + \begin{pmatrix} -\Delta v_0 \bar{w}_0 \\ \Delta u_0 \bar{w}_0 \end{pmatrix} \right] = \nabla_H \cdot \begin{pmatrix} -\Delta v_0 \bar{w}_0 \\ \Delta u_0 \bar{w}_0 \end{pmatrix}, \quad (36)$$

²⁷⁴ or

$$\nabla_H \cdot [\overline{\boldsymbol{\omega}}_{H0} \bar{w}_0] = \frac{\alpha \gamma^2}{12} \nabla_H \cdot [(\nabla_H b_0 + \alpha \mathbf{k} \times \nabla_H b_0) \nabla_H^2 b_0]. \quad (37)$$

²⁷⁵ using the leading order velocities. The last two flux terms involving departures from the mean

²⁷⁶ vorticity are

$$\nabla_H \cdot [\overline{u'_{H0} \zeta'_0}] = -\frac{\gamma^2}{12} \nabla_H \cdot [(\alpha \nabla_H b_0 - \mathbf{k} \times \nabla_H b_0) \nabla_H^2 b_0], \quad (38)$$

²⁷⁷ and

$$\nabla_H \cdot [\overline{\omega'_{H0} w'_0}] = \nabla_H \cdot \begin{pmatrix} \frac{1}{2} \frac{\partial}{\partial y} [\overline{w'_0}^2] - \frac{\partial \bar{v}'_0}{\partial z} \overline{w'_0} \\ -\frac{1}{2} \frac{\partial}{\partial x} [\overline{w'_0}^2] + \frac{\partial \bar{u}'_0}{\partial z} \overline{w'_0} \end{pmatrix} = \nabla_H \cdot \begin{pmatrix} -\frac{\partial \bar{v}'_0}{\partial z} \overline{w'_0} \\ \frac{\partial \bar{u}'_0}{\partial z} \overline{w'_0} \end{pmatrix} = \mathbf{0}, \quad (39)$$

²⁷⁸ since u'_0 and v'_0 are linear in z and $\bar{w}' = 0$. The terms in $\overline{w'_0}^2$ can be written as a curl and hence are
²⁷⁹ divergence free.

²⁸⁰ Combining these results, the vertical vorticity equation can be written

$$\frac{\partial \nabla_H^2 \psi_0}{\partial t} + J(\psi_0, \nabla_H^2 \psi_0) = \frac{\gamma^2}{12} \nabla_H \cdot [(2\alpha \nabla_H b_0 + (\alpha^2 - 1) \mathbf{k} \times \nabla_H b_0) \nabla_H^2 b_0]. \quad (40)$$

281 The left hand side of Eq. 40 corresponds to advection of vertical vorticity. The first term in brackets
 282 on the right hand side corresponds to a cross-front vorticity flux, and the second term in brackets
 283 corresponds to an along-front skew flux.

284 *c. The Skew Flux Term*

285 As mentioned earlier, a skew flux term appears in the evolution equation for b_0 (the second
 286 term on the right hand side of Eq. 27). This term, $\mathcal{J}_b = -\mathbf{k} \times \nabla_H b_0 |\nabla_H b_0|^2$, represents a flux of
 287 buoyancy perpendicular to the buoyancy gradient. As noted above, a skew flux also appears in the
 288 vertical vorticity equation (Eq. 40) which we will denote $\mathcal{J}_v = (\mathbf{k} \times \nabla_H b_0) \nabla_H^2 b_0$.

289 The divergence of the skew flux terms in the buoyancy and vorticity equations can be re-
 290 expressed in terms of advection operators. First, note that the divergence of the skew flux terms
 291 can be written as

$$\nabla_H \cdot \mathcal{J}_b = -\nabla_H \cdot [\mathbf{k} \times \nabla_H b_0 |\nabla_H b_0|^2] = -\nabla_H b_0 \cdot [-\mathbf{k} \times \nabla_H |\nabla_H b_0|^2], \quad (41)$$

292 and

$$\nabla_H \cdot \mathcal{J}_v = \nabla_H \cdot [(\mathbf{k} \times \nabla_H b_0) \nabla_H^2 b_0] = -\nabla_H b_0 \cdot [(\mathbf{k} \times \nabla_H) \nabla_H^2 b_0]. \quad (42)$$

293 Therefore, the terms in brackets can be written in the form of advection operators with velocities

$$\mathbf{u}_b = -\mathbf{k} \times \nabla_H |\nabla_H b_0|^2 = \nabla_H \times [|\nabla_H b_0|^2 \mathbf{k}], \quad (43)$$

294 and

$$\mathbf{u}_v = (\mathbf{k} \times \nabla_H) \nabla_H^2 b_0 = \nabla_H \times [-\nabla_H^2 b_0 \mathbf{k}]. \quad (44)$$

295 Therefore \mathbf{u}_b and \mathbf{u}_v can be written in terms of streamfunctions, $\chi_b = -|\nabla_H b_0|^2$ and $\chi_v = \nabla_H^2 b_0$.
 296 In the buoyancy equation the skew flux term can be combined with the existing advection term,
 297 $J(\psi_0, b_0)$. From the form of the streamfunction, χ_b , we see that the effect of the skew flux term,

²⁹⁸ \mathcal{J}_b , is to advect buoyancy along the contours of $|\nabla_H b_0|^2 = \text{const}$. Equations 27 and 40 can then be
²⁹⁹ written

$$\frac{\partial b_0}{\partial t} + J\left(\psi_0 - \frac{\sqrt{\text{Ro}}\mathcal{P}\gamma^2}{12}|\nabla_H b_0|^2, b_0\right) = \frac{\text{Ro}\text{Pr}_\alpha\alpha\gamma^2}{12}\nabla_H \cdot [\nabla_H b_0|\nabla_H b_0|^2] + O(\text{Ro}), \quad (45)$$

³⁰⁰ and

$$\frac{\partial \nabla_H^2 \psi_0}{\partial t} + J(\psi_0, \nabla_H^2 \psi_0) + \frac{(\alpha^2 - 1)\gamma^2}{12}J(\nabla_H^2 b_0, b_0) = \frac{2\alpha\gamma^2}{12}\nabla_H \cdot [\nabla_H b_0 \nabla_H^2 b_0]. \quad (46)$$

³⁰¹ Note that using Equation 45 with $\text{Pr}_\alpha = \mathcal{P}/\sqrt{\text{Ro}}$ corresponds to the Young (1994) case. In the
³⁰² $\text{Pr}_\alpha = O(1)$ limit that we consider, only the vorticity skew flux term, \mathcal{J}_v , enters the equations at
³⁰³ leading order and the advection of buoyancy by the buoyancy skew flux term, \mathcal{J}_b , is small.

³⁰⁴ d. Horizontal Diffusion

³⁰⁵ The system described by Eqns. 1a-1e parameterizes vertical mixing by relaxing the velocity and
³⁰⁶ buoyancy fields towards their local depth average, but the equations do not include any parameteri-
³⁰⁷ zation for horizontal mixing by small-scale turbulence. As will be shown below, the most unstable
³⁰⁸ mode in this system has an infinite horizontal wavenumber or, equivalently, a vanishingly small
³⁰⁹ wavelength. Fortunately, it is relatively straightforward to include a parameterization of horizontal
³¹⁰ mixing using horizontal Laplacian viscous and diffusive terms with viscosity ν and diffusivity κ .

³¹¹ The addition of these terms shifts the most unstable mode to a finite wavenumber. Note that this
³¹² Laplacian scheme differs from the relaxation parameterization used to represent vertical mixing
³¹³ and is used for mathematical convenience. Appendix C describes a model with Laplacian mixing
³¹⁴ schemes in the horizontal and vertical directions.

³¹⁵ With the addition of parameterized horizontal mixing, the terms $\epsilon^2 E \nabla_H^4 \psi_0$ and $\epsilon^2 E / \text{Pr}_E \nabla_H^2 b_0$
³¹⁶ appear on the right hand sides of the depth-averaged vorticity and buoyancy equations, respec-
³¹⁷ tively, where recall that $\epsilon = H/L$ is the aspect ratio, $E = \nu/(fH^2)$ is the Ekman number and

³¹⁸ $\text{Pr}_E = v/\kappa$ is the Prandtl number. In most applications $\varepsilon \ll 1$ and these terms will be small.
³¹⁹ However, for very small Ro these terms might contribute significantly. Writing $\mathcal{E} = \varepsilon^2 E/\text{Ro}$, the
³²⁰ resulting equations are

$$\frac{\partial b_0}{\partial t} + J(\psi_0, b_0) = \left[\frac{\alpha \gamma N^2}{12} + \frac{\mathcal{E}}{\text{Pr}_E} \right] \nabla_H^2 b_0, \quad (47)$$

³²¹ and

$$\frac{\partial \nabla_H^2 \psi_0}{\partial t} + J(\psi_0, \nabla_H^2 \psi_0) - \mathcal{E} \nabla_H^4 \psi_0 = \frac{\gamma^2}{12} \nabla_H \cdot [(2\alpha \nabla_H b_0 + (\alpha^2 - 1) \mathbf{k} \times \nabla_H b_0) \nabla_H^2 b_0], \quad (48)$$

³²² which are asymptotically valid if $\varepsilon^2 E = O(\text{Ro})$. For convenience, we will write the combined
³²³ buoyancy diffusivity appearing in Eq. 47 as

$$\mathcal{D} = \left[\frac{\alpha \gamma N^2}{12} + \frac{\mathcal{E}}{\text{Pr}_E} \right]. \quad (49)$$

³²⁴ We note that these equations can be obtained from Young (1994) in the limit of fast buoyancy
³²⁵ mixing ($1/\mu_b \ll L/U$). However this result would only strictly be valid for small α based on the
³²⁶ analysis in Young (1994) due to the use of different asymptotic limits, while here no constraints
³²⁷ have been placed on the size of α .

³²⁸ 5. Instabilities of the Depth-Averaged Equations

³²⁹ Equations 47 and 48 are a closed system of equations for the leading order buoyancy and vorticity.
³³⁰ In this section, we will analyze the stability of these equations to small amplitude disturbances.
³³¹ For simplicity, we will consider perturbations about a basic state where buoyancy is a linear function
³³² of x , i.e. $b_0 = Bx$ for a constant B , and where the vertical vorticity is zero. Introducing normal
³³³ mode perturbations of the form $\exp[i(kx + ly) + \sigma t]$, the total buoyancy and vorticity can be written
³³⁴ using an eigenmode decomposition,

$$(b_0, \psi_0) = (\delta A \exp[i(kx + ly) + \sigma t] + Bx, \delta C \exp[i(kx + ly) + \sigma t]), \quad (50)$$

335 for wavevector (k, l) , growth rate σ and small parameter δ . The vector (A, C) is the eigenvector of
 336 the resulting linear system.

337 To leading order in δ , the linearized buoyancy and vorticity equations can be written

$$\sigma A - ilBC = -(k^2 + l^2)\mathcal{D}A, \quad (51)$$

338 and

$$-\sigma(k^2 + l^2)C = \frac{\gamma^2}{12}[-2\alpha ik(k^2 + l^2) - (\alpha^2 - 1)il(k^2 + l^2)]BA + (k^2 + l^2)^2\mathcal{E}C, \quad (52)$$

339 or in the form of a single matrix equation,

$$\begin{pmatrix} \sigma + (k^2 + l^2)\mathcal{D} & -lB \\ \frac{\gamma^2}{12}[2\alpha k + (\alpha^2 - 1)l]B & \sigma + (k^2 + l^2)\mathcal{E} \end{pmatrix} \begin{pmatrix} A \\ iC \end{pmatrix} = \mathbf{0}. \quad (53)$$

340 For this equation to be valid for some non-zero vector (A, iC) , the determinant of this matrix must
 341 vanish. Therefore

$$[\sigma + (k^2 + l^2)\mathcal{D}][\sigma + (k^2 + l^2)\mathcal{E}] + \frac{\gamma^2 B^2}{12}[2\alpha kl + (\alpha^2 - 1)l^2] = 0. \quad (54)$$

342 The solution to this equation for the growth rate, σ , is

$$\sigma_{\pm} = -\frac{\mathcal{D} + \mathcal{E}}{2}(k^2 + l^2) \pm \sqrt{\left[\frac{\mathcal{D} - \mathcal{E}}{2}\right]^2(k^2 + l^2)^2 - \mathcal{B}^2[2\alpha kl + (\alpha^2 - 1)l^2]}, \quad (55)$$

343 where $\mathcal{B}^2 = \gamma^2 B^2 / 12$ is a re-scaled buoyancy gradient and the parameters

$$\mathcal{D} = \frac{\alpha \gamma Bu}{12 \text{Ro}} + \frac{\mathcal{E}}{\text{Pr}_E}, \quad \mathcal{E} = \frac{\varepsilon^2 E}{\text{Ro}}, \quad (56)$$

344 can be written in terms of the non-dimensional numbers defined in Table 1. The growth rate has a
 345 maximum at a finite wavevector (k, l) . Note that in the case where $\mathcal{D} = \mathcal{E}$ (e.g. with $\mathcal{N}^2 = 0$ and
 346 $\text{Pr}_E = 1$), the growth rate simplifies to

$$\sigma_{\pm} = -\mathcal{E}(k^2 + l^2) \pm \mathcal{B}\sqrt{-[2\alpha kl + (\alpha^2 - 1)l^2]}. \quad (57)$$

³⁴⁷ To find the maximum growth rate in the more general case, it is useful to define a rotated wavevector,
³⁴⁸ $\mathbf{l}' = \mathbf{R}_\alpha \mathbf{l}$, where $\mathbf{l} = (k, l)$ and the rotation matrix,

$$\mathbf{R}_\alpha = \frac{1}{\sqrt{1+\alpha^2}} \begin{pmatrix} 1 & \alpha \\ -\alpha & 1 \end{pmatrix}, \quad (58)$$

³⁴⁹ is orthogonal with determinant 1 corresponding to a rotation by $\theta = -\arctan \alpha$. The growth rate
³⁵⁰ in rotated coordinates becomes

$$\sigma_\pm = -\frac{\mathcal{D} + \mathcal{E}}{2}(k'^2 + l'^2) \pm \sqrt{\left[\frac{\mathcal{D} - \mathcal{E}}{2}\right]^2 (k'^2 + l'^2)^2 + \mathcal{B}^2 [l'^2 - \alpha^2 k'^2]}. \quad (59)$$

³⁵¹ For a fixed wavelength, the growth rate in Eq. 59 is maximum for $(k', l') = (0, \pm K)$, corresponding
³⁵² to waves aligned at an angle of $\arctan \alpha$ to the down-front (y) direction. We note that the fastest
³⁵³ growing modes therefore have a wavevector aligned with the horizontal velocity at the top and
³⁵⁴ bottom boundaries. The same is true for the the classical Eady instability where the wavenumber
³⁵⁵ of the fastest growing modes is in the down-front direction (Eady 1949; Vallis 2006), but here
³⁵⁶ the cross-front flow changes the orientation of the growing modes with respect to the front. The
³⁵⁷ maximum growth rate over all directions as a function of the wavenumber is therefore

$$\sigma_{max}(K) = -\frac{\mathcal{D} + \mathcal{E}}{2} K^2 + \sqrt{\left[\frac{\mathcal{D} - \mathcal{E}}{2}\right]^2 K^4 + \mathcal{B}^2 K^2}. \quad (60)$$

³⁵⁸ Maximizing over K , the most unstable mode has a growth rate

$$\max_K [\sigma_{max}] = \frac{\mathcal{B}^2}{(\sqrt{\mathcal{D}} + \sqrt{\mathcal{E}})^2}, \quad (61)$$

³⁵⁹ which reduces to $\max_K [\sigma_{max}] = \mathcal{B}^2 / (4\mathcal{D})$ in the case $\mathcal{D} = \mathcal{E}$. Therefore the most unstable
³⁶⁰ wavenumber, K_{max} satisfies

$$K_{max}^2 = \frac{-2\mathcal{D}\mathcal{E} + \sqrt{\mathcal{D}\mathcal{E}(\mathcal{D} + \mathcal{E})^2}}{\mathcal{D}\mathcal{E}(\mathcal{D} - \mathcal{E})^2} \mathcal{B}^2, \quad (62)$$

³⁶¹ which reduces to

$$K_{max}^2 = \frac{\mathcal{B}^2}{4\mathcal{D}^2}, \quad (63)$$

362 in the case $\mathcal{D} = \mathcal{E}$.

363 As noted above, the horizontal viscous/diffusion terms are necessary to produce a finite
364 wavenumber maximum since $K_{max}^2 \rightarrow \infty$ as $\mathcal{E} \rightarrow 0$. Therefore, the system without horizontal
365 viscosity and diffusion appears to produce an ‘ultraviolet catastrophe’. However, the maximum
366 growth rate in this case does remain bounded since σ_{max} asymptotes to $\mathcal{B}^2/\mathcal{D}$ for large K^2 .

367 The case of $\mathcal{D} = 0$ and $\mathcal{E} \neq 0$ corresponds to no stratification and an infinite Prandtl number. By
368 symmetry in \mathcal{E} and \mathcal{D} this case is the same as the $\mathcal{E} = 0$ case though with different eigenvectors.

369 When both \mathcal{E} and \mathcal{D} are zero, corresponding to no stratification and no horizontal diffusion, we
370 have

$$\sigma_{max}(K) = \mathcal{B}K, \quad (64)$$

371 so the growth rate is unbounded and waves with infinite wavenumber will grow infinitely quickly.

372 The case of $\alpha = 0$ corresponds to the small wavenumber (long wave) limit of the classical Eady
373 problem, where the growth rate is

$$\sigma_{Eady} = \frac{Bl}{\mu} \left[\left(\coth \frac{\mu}{2} - \frac{\mu}{2} \right) \left(\frac{\mu}{2} - \tanh \frac{\mu}{2} \right) \right]^{1/2}, \quad (65)$$

374 for scaled wavenumber $\mu^2 = Bu l^2$ (Vallis 2006). Since we consider $Bu = O(\text{Ro})$, the relevant
375 limit is the small μ limit in which case σ_{Eady} reduces to

$$\sigma_{Eady} \sim \frac{Bl}{\sqrt{12}} = \mathcal{B}K, \quad (66)$$

376 consistent with Eq. 64. Note that this result is independent of the background buoyancy gradient
377 represented by Bu . This result is also consistent with the small K limit of ageostrophic baroclinic
378 instability considered by Stone (1966).

379 As noted earlier, the direction of the most unstable modes described by Eq. 59 corresponds to
380 $k' = 0$. In non-rotated coordinates this corresponds to $k = -\alpha l$, where k is the wavenumber in the
381 cross-front direction and l is the wavenumber in the along-front direction. In contrast, the most

382 unstable modes in the inviscid Eady problem have $k = 0$ and hence correspond to the limit of
383 $\alpha \rightarrow 0$.

384 Instead, the modes perpendicular to the most unstable modes have $l = \alpha k$ in non-rotated coordinates.
385 For these modes, the coefficient multiplying B^2 inside the square root in Eq. 59 is negative.
386 If $\mathcal{E} = \mathcal{D}$, σ_{\pm} is purely imaginary for these modes, corresponding to traveling waves with a con-
387 stant amplitude. Note, however, that the neglected higher order terms could add a real part to
388 this growth rate and hence cause these perturbations to grow, while adding horizontal friction and
389 diffusion will cause them to slowly decay with faster decay at higher wavenumbers.

390 Figure 1 shows the real and imaginary parts of σ_{\pm} in the case of no horizontal friction and
391 diffusion or background stratification ($\mathcal{D} = \mathcal{E} = 0$). Only the σ_+ branch produces growing modes
392 with the fastest growth occurring for large K along the line $k = -\alpha l$. Figure 2 shows the real and
393 imaginary parts of σ_{\pm} with $\mathcal{E} = \mathcal{D} = 2.5 \times 10^{-3}$, corresponding to large horizontal friction and
394 diffusivity or small Rossby number. A maximum in the growth rate can be seen on the plot of
395 $Re[\sigma_+]$ for $K_{max} = 92.4$ along the line $k = -\alpha l$.

396 We anticipate that the ‘ultraviolet catastrophe’ in the system without horizontal mixing will be
397 cured by finite Rossby number effects. Equations 45 and 46 contain terms that are $O(\text{Ro})$ which
398 were neglected in equations 47 and 48. These terms involve an extra power of the horizontal
399 wavenumber magnitude, K , compared to the leading order terms. Therefore, the neglect of these
400 terms is asymptotically valid when $K \ll O(1/\text{Ro})$. For sufficiently large K the neglected $O(\text{Ro})$
401 terms will become important and modify the growth rate, possibly resulting in a maximum growth
402 rate at a lower wavenumber than predicted in Eq. 62 when the Rossby number is not infinitesimally
403 small. This will be discussed further in §7.

404 **6. Numerical Simulations**

405 To test the theory described above, we have conducted a series of fully nonlinear numerical sim-
406 ulations using the code DIABLO. The code solves the incompressible non-hydrostatic Boussinesq
407 equations. Time stepping is performed with a combination of explicit third-order Runge-Kutta and
408 implicit Crank Nicolson schemes while finite differences are used for derivatives in the vertical di-
409 rection and discrete Fourier transforms, using the pseudo-spectral method for non-linear terms, are
410 used for derivatives in the horizontal direction (Taylor 2008).

411 The simulations solve the non-dimensional equations where x , y , and z are normalized by the
412 size of the computational domain such that the non-dimensional domain size is $L_x = L_y = L_z = 1$.
413 The boundary conditions in the vertical direction are no stress, no buoyancy flux and no vertical
414 velocity on the top and bottom surfaces. Periodic boundary conditions are applied to the velocity
415 in both horizontal directions (see below for buoyancy).

416 For numerical stability, viscous terms of the form

$$D_{(u,v)} = E \left(\frac{\partial^2}{\partial z^2} + \varepsilon^2 \nabla_H^2 \right) (u, v), \quad (67)$$

$$D_w = \varepsilon^2 E \left(\frac{\partial^2}{\partial z^2} + \varepsilon^2 \nabla_H^2 \right) w, \quad (68)$$

418 and

$$D_b = \frac{E}{Pr_E} \left(\frac{\partial^2}{\partial z^2} + \varepsilon^2 \nabla_H^2 \right) b, \quad (69)$$

419 are added to the horizontal momentum, vertical momentum and buoyancy equations respectively.
420 The simulations use a small Ekman number, E , and a small aspect ratio, ε , such that the dominant
421 vertical mixing process is the relaxation to the depth-average. The simulations are initialized with
422 the solution given in Appendix B with vertical diffusion and relaxation. For the small Ekman
423 numbers considered here this solution exhibits thin boundary layers where vertical diffusion is
424 important. Outside of these boundary layers, the velocity and buoyancy fields correspond to the

425 solution given in §3. The initial velocity field is set to the leading order solution while the initial
426 buoyancy field is prescribed to be a linear horizontal background gradient plus the resulting $O(\text{Ro})$
427 correction.

428 Periodic boundary conditions are inconsistent with the initial conditions for buoyancy which
429 have a constant horizontal buoyancy gradient. To overcome this, we decompose the total buoyancy
430 into a background term with a constant buoyancy gradient and departures from this gradient, i.e.

$$b = Bx + b_p, \quad (70)$$

431 where B is constant. This form is inserted into the buoyancy equation, and periodic boundary
432 conditions are applied to b_p . This has the effect of fixing the change in buoyancy across the
433 domain in the x direction. A similar approach has been used in a number of previous studies (e.g.
434 Taylor and Ferrari (2011); Taylor (2016)).

435 Small amplitude normal mode perturbations are then added the buoyancy and streamfunction of
436 the form

$$b'_0 = \mathcal{R} \left[\sum_{(k,l)} A_{kl} \exp[i(kx + ly + \phi_{kl})] \right], \quad (71)$$

437 and

$$\psi'_0 = \mathcal{R} \left[\sum_{(k,l)} C_{kl} \exp[i(kx + ly + \phi_{kl})] \right], \quad (72)$$

438 where ϕ_{kl} is a random phase, $\mathcal{R}[f]$ denotes the real part of f and $(k,l) = 2\pi(n_k, n_l)$ for $n_{k,l} = 1, 2, \dots$
439 and $n_k^2 + n_l^2 < N_{max}^2$ describing a disc in phase space of radius $2\pi N_{max}$.

440 Note that the leading order depth-dependent velocity depends on b_0 and hence the velocity
441 perturbation can be found from b'_0 , while perturbations to the depth-independent velocity are in-
442 troduced through ψ'_0 . Similarly, the leading order depth-dependent buoyancy, b_1 , depends on b_0
443 and therefore perturbations to b_1 are introduced through b'_0 . In the simulations, we set the ampli-
444 tudes $|A_{kl}| = |C_{kl}| = 10^{-12}$ which ensure an interval of linear perturbation growth, while the phase

445 difference between A_{kl} and C_{kl} is randomized. We use a background buoyancy gradient of $B = 2$
446 such that $b = \pm 1$ at $x = \pm 0.5$.

447 There are several non-dimensional parameters in the system described here. For simplicity, the
448 numerical simulations are conducted for fixed Burger number, Prandtl number, aspect ratio, and
449 Ekman numbers, with $Bu = 0$, $Pr_\alpha = Pr_E = 1$, $\epsilon = 0.05$ and $E = 10^{-4}$. The Rossby number,
450 Ro , and relaxation ratio, α , are varied over the set of values $Ro \in \{10^{-4}, 10^{-3}, 10^{-2}, 10^{-1}\}$ and
451 $\alpha \in \{0, 0.2, 0.4, 0.6, 0.8, 1\}$. Each simulation is run until growing modes develop and transition to
452 a nonlinear state.

453 *a. Description*

454 First, we compare the linear instabilities captured by the numerical simulations with the pre-
455 dictions from the theory outlined above. We find that for sufficiently small Rossby numbers, the
456 predicted angles of the instability and growth rates closely match the analytical predictions. This
457 is perhaps not surprising since the theory is developed in the limit of asymptotically small Rossby
458 number. However, by comparing the simulations and theory, we can quantify how large the Rossby
459 number can be before the analytical theory breaks down.

460 Figure 3 illustrates the development and nonlinear breakdown of the unstable modes from a
461 simulation with $Ro = 10^{-3}$ and $\alpha = 0.4$. Here, the depth-averaged buoyancy field is plotted,
462 where the background buoyancy gradient, B , has been removed. For reference, the unperturbed
463 basic state is $\bar{b} = Bx$, which would have vertical buoyancy contours in this figure. At a relatively
464 early time ($t = 0.314$, upper right panel), growing perturbations develop with a distinctive angle
465 with respect to the buoyancy gradient. Note that the fastest growing modes occur on a larger scale
466 compared to the initial perturbations, suggesting a scale-selective process. By $t = 0.384$ (lower
467 left panel) the flow transitions to a nonlinear regime and the growing perturbations roll up into

468 coherent vortices. These vortices then merge resulting in an energy cascade to larger scales (see
469 lower right panel).

470 Figure 4 shows two simulations with different values of α during the period when the perturba-
471 tions are linear and the growth is exponential. The theoretical prediction for the direction of the
472 fastest growing modes, $k = -\alpha l$, is plotted as a black dashed line. As predicted, the wave crests
473 of the most unstable modes are nearly perpendicular to the predicted wavenumber vector.

474 Figure 5 shows the buoyancy perturbation from four simulations with different values of the
475 Rossby number. In all cases, $\alpha = 0.4$, and hence the predicted angle of the most unstable modes
476 is the same. The wavelength of the most unstable modes changes with Ro, but interestingly the
477 dependence is not monotonic. For the range of Ro tested, the shortest waves are observed for
478 $\text{Ro} = 10^{-3}$. For $\text{Ro} = 10^{-4} - 10^{-2}$ the direction of the wavevector is independent of Ro and
479 closely matches the theoretical prediction.

480 In the case with the largest Rossby number, $\text{Ro} = 0.1$, the fastest growing mode does not fit
481 in the domain, and instead a quantized mode with $(k, l) = (0, 2\pi)$ appears. There also appear to
482 be growing perturbations at an angle nearly perpendicular to the analytical prediction of $k = -\alpha l$.
483 These modes might be an indication of symmetric instability modified by vertical mixing, although
484 this is not captured by our theory and we do not focus on it here.

485 *b. Energetics*

486 To describe the dynamics of the unstable modes, it is useful to diagnose the perturbation energy
487 budgets. To start, we define the horizontal domain average to be

$$\langle f \rangle = \int_{-0.5}^{0.5} \int_{-0.5}^{0.5} f dx dy, \quad (73)$$

⁴⁸⁸ and let $\tilde{f} = f - \langle f \rangle$ denote the departure from the horizontal average. The nondimensional energy
⁴⁸⁹ equation can be derived from the governing equations and written in conservative form as

$$\text{Ro} \frac{\partial \mathcal{K}}{\partial t} + \nabla \cdot [(\text{Ro} \mathcal{K} + p) \mathbf{u}] - b w = -\alpha (u u' + v v') , \quad (74)$$

⁴⁹⁰ for kinetic energy density

$$\mathcal{K} = \frac{1}{2} (u^2 + v^2 + \varepsilon^2 w^2) , \quad (75)$$

⁴⁹¹ assuming that the diffusive terms are small. We now consider the perturbation kinetic energy,

$$e = \frac{1}{2} \langle \tilde{u}^2 + \tilde{v}^2 + \varepsilon^2 \tilde{w}^2 \rangle , \quad (76)$$

⁴⁹² and using Eq. 74 and the horizontally averaged governing equations, the perturbation energy bud-
⁴⁹³ get can be written

$$\begin{aligned} \text{Ro} \left[\underbrace{\frac{\partial e}{\partial t} + \langle w \rangle \frac{\partial e}{\partial z} + \langle \tilde{u} \tilde{w} \rangle \frac{\partial \langle u \rangle}{\partial z} + \langle \tilde{v} \tilde{w} \rangle \frac{\partial \langle v \rangle}{\partial z}}_{\mathcal{S}} + \underbrace{\frac{1}{2} \frac{\partial}{\partial z} \langle [\tilde{u}^2 + \tilde{v}^2 + \varepsilon^2 \tilde{w}^2] \tilde{w} \rangle}_{\mathcal{T}} \right] = \\ \underbrace{- \frac{\partial}{\partial z} \langle \tilde{p} \tilde{w} \rangle}_{\mathcal{P}} + \underbrace{\langle \tilde{b} \tilde{w} \rangle}_{\mathcal{B}} - \underbrace{\alpha \langle \tilde{u}' \tilde{u} + \tilde{v}' \tilde{v} \rangle}_{\mathcal{R}} . \end{aligned} \quad (77)$$

⁴⁹⁴ The terms in Eq. 77 can be interpreted as \mathcal{S} : production of perturbation kinetic energy by the mean
⁴⁹⁵ shear, \mathcal{T} : turbulent transport, \mathcal{P} : pressure transport, \mathcal{B} : buoyancy flux, and \mathcal{R} : dissipation by the
⁴⁹⁶ parameterized vertical mixing. From mass conservation $\partial \langle w \rangle / \partial z = 0$ and hence $\langle w \rangle = \text{const.}$ and
⁴⁹⁷ using the vertical boundary conditions we have that $\langle w \rangle = 0$. We can now vertically average Eq.
⁴⁹⁸ 77 to remove the transport terms. The resulting equation for the domain averaged perturbation
⁴⁹⁹ kinetic energy is

$$\text{Ro} \frac{\partial \bar{e}}{\partial t} = \bar{\mathcal{S}} + \bar{\mathcal{F}} + \bar{\mathcal{R}} . \quad (78)$$

⁵⁰⁰ The depth-averaged dissipation associated with the vertical relaxation term is given by

$$\bar{\mathcal{R}} = -\alpha \left[\overline{\langle \tilde{u}'^2 \rangle} + \overline{\langle \tilde{v}'^2 \rangle} \right] = -\alpha \left[\overline{\langle \tilde{u}^2 \rangle} + \overline{\langle \tilde{v}^2 \rangle} - \overline{\langle \tilde{u}^2 \rangle} - \overline{\langle \tilde{v}^2 \rangle} \right] , \quad (79)$$

501 which is negative by the Cauchy-Schwarz inequality. We now calculate the four terms in Eq. 78
502 using our numerical data and consider the energy balance in order to determine the energy source
503 and mechanism for the instability.

504 Figure 6 shows the four terms in Eq. 78 for four different values of (Ro, α) . Clear regions of
505 exponential growth (with constant slope on the semi-log plot) develop in each case. When $\alpha = 0$,
506 corresponding to the classical Eady model, we can see that the dominant energy balance is between
507 the time rate of change in kinetic energy and the buoyancy flux, representing the transformation
508 of perturbation potential energy into perturbation kinetic energy and indicative of baroclinic in-
509 stability. For nonzero α , the dominant balance is between the buoyancy flux and the dissipation
510 associated with the vertical relaxation term, with the residual corresponding to the time rate of
511 change of kinetic energy. Therefore, in the presence of vertical mixing, the instability is driven
512 by a transfer of potential energy from the buoyancy field consistent with baroclinic instability,
513 although most of the energy extracted from the potential energy reservoir is dissipated through
514 the vertical mixing (relaxation) term. We note that the balance between $\bar{\mathcal{F}}$ and $\bar{\mathcal{R}}$ is closer for
515 smaller Ro which is consistent with the asymptotic theory. Once the instability reaches the non-
516 linear phase, the neglected viscous dissipation term becomes significant due to the appearance of
517 small scale vortices.

518 *c. Growth Rate*

519 In this section, we diagnose the growth rate of the unstable perturbations from the numerical
520 simulations and compare these with the prediction from the analytical theory. We define the growth
521 rate of perturbations captured in the numerical simulations by

$$\sigma_N = \frac{1}{2\bar{e}} \frac{d\bar{e}}{dt}. \quad (80)$$

522 This can then be compared with the theoretical growth rate, σ , given by the eigenmode decompo-
 523 sition in Eq. 50. We now define $\sigma_{avg}(t_1, t_2)$ to be the average of σ_N in the time interval $[t_1, t_2]$ and
 524 $\sigma_{rms}(t_1, t_2)$ to be the RMS deviation from this average. Specifically,

$$\sigma_{avg}(t_1, t_2) = \frac{1}{t_2 - t_1} \int_{t_1}^{t_2} \sigma_N(t) dt, \quad (81)$$

525 and

$$\sigma_{rms}(t_1, t_2) = \left[\frac{1}{t_2 - t_1} \int_{t_1}^{t_2} [\sigma_N(t) - \sigma_{avg}(t_1, t_2)]^2 dt \right]^{1/2}. \quad (82)$$

526 We define the interval of exponential growth to be the largest time interval in which the ratio of
 527 σ_{rms} to σ_{avg} is below a specified tolerance, i.e. $\sigma_{rms}/\sigma_{avg} < \delta$. The value of the growth rate is then
 528 taken to be σ_{avg} within the region of exponential growth. We use a tolerance of $\delta = 0.01$ and do
 529 not define a growth rate if the region of exponential growth is small or σ_N is strongly oscillatory.
 530 We also use 2D discrete Fourier transforms to determine the wavevector of the fastest growing
 531 modes in each simulation.

532 As an illustration of this procedure, Figure 7 shows σ_N diagnosed from four simulations with
 533 different values of Ro and α . For large Ro , large oscillations in σ_N prevent us from accurately
 534 diagnosing the growth rate for $\alpha > 0.6$. Figure 8 shows the growth rate and wavenumber of the
 535 fastest growing modes diagnosed in this way for each simulation. We exclude results for large Ro
 536 and α where we are unable to accurately diagnose the growth rate. For $Ro = 0.1$ the dominant
 537 mode is $(k, l) = (0, 2\pi)$ which is likely not the fastest growing mode due to the restrictions of the
 538 domain size. For small Rossby number, the wavenumber of the fastest growing mode depends
 539 on α while for $Ro \geq 10^{-3}$ it is independent of α . This is an indication that there are different
 540 processes controlling the most unstable modes for small and large Ro .

541 Figure 9 shows the 2D Fourier transform of the depth-averaged buoyancy perturbation for sev-
 542 eral values of Ro and α . When viscous effects are included the wavenumber associated with the

543 most unstable mode is given by 63 and can be written as

$$K_{max} = \frac{\text{Ro}B}{\sqrt{48}(1+\alpha^2)\varepsilon^2 E}, \quad (83)$$

544 by taking $\text{Pr}_E = 1$ and $\text{Bu} = 0$. The dependence of K_{max} on α matches the simulations for
545 $\text{Ro} = 10^{-4}$ (see Figure 8). The circles on Figure 9 have radius given by Eq. 83 and we can see
546 that the numerical results match the predictions of fastest growing wavenumber for $\text{Ro} = 10^{-4}$.
547 However, for larger Ro the fastest growing wavenumber is significantly smaller than the theoretical
548 prediction. It appears that there is a second, α independent effect which controls the fastest
549 growing modes and is not captured by the theory. This will be examined further in §7. Note from
550 Eq. 83 that K_{max} depends on the aspect ratio, ε , when viscous effects set the scale of the most
551 unstable mode. However, as seen in Figure 8, the scale of the most unstable mode for $\text{Ro} > 10^{-3}$
552 appears to be independent of viscosity (and independent of the aspect ratio).

553 Along the direction $k = -\alpha l$, the growth rate is given by Eq. 60. For $\text{Bu} = 0$ and $\text{Pr}_E = 1$, the
554 growth rate of the most unstable mode given in Eq. 60 can be written

$$\sigma_{max} = \frac{BK}{\sqrt{12}(1+\alpha^2)} - \frac{\varepsilon^2 E K^2}{\text{Ro}}. \quad (84)$$

555 Figure 10 shows a comparison between the growth rates predicted by Eq. 84 (left panel) and
556 the growth rates diagnosed from the numerical simulations (right panel) where the wavenumber
557 corresponding to the most unstable mode as diagnosed in the numerical simulations is used to set K
558 in Eq. 84. There is very good agreement between the growth rates from the theory and simulations
559 across a wide range of Rossby numbers and relaxation ratios. Interestingly, the growth rates match
560 reasonably well even in cases where the most unstable wavenumber in the theory (Eq. 83) doesn't
561 match the most unstable wavenumber diagnosed in the simulations (e.g. the cases in the bottom
562 panels of Figure 9).

563 **7. QG analysis of a stratified basic state**

564 The numerical simulations described above indicate that the wavenumber of the most unstable
 565 mode is set by a process other than viscosity for the larger values of Ro. In this section we
 566 use the quasi-geostrophic (QG) equations to examine the stability of a depth-dependent basic
 567 state associated with vertical mixing of momentum and buoyancy. Specifically the velocity and
 568 buoyancy of the basic state will be given by Eqns. 16 and 19. Importantly, here the stratification of
 569 the basic state is non-zero and is the result of a balance between cross-front advection and vertical
 570 mixing. Since the stratification in Eq. 19 appears at $O(\text{Ro})$, it did not appear in the basic state
 571 analyzed in §5. Here, we also assume that departures from the basic state are not directly affected
 572 by vertical or horizontal mixing. This allows us to isolate the influence of vertical mixing on the
 573 background flow from its influence on the growing perturbations.

574 The total velocity and buoyancy fields can be written as

$$(u, v, w, b) = (U + \hat{u}, V + \hat{v}, \hat{w}, Bx + N^2 z + \hat{b}), \quad (85)$$

575 where capital letters denote the basic state and $\hat{\cdot}$ denotes a perturbation to the basic state. The
 576 nondimensional QG equation can be written

$$\left[\frac{\partial^2}{\partial x^2} + \frac{\partial^2}{\partial y^2} + \frac{1}{\text{Ro}} \frac{\partial}{\partial z} \left(\frac{1}{N^2} \frac{\partial}{\partial z} \right) \right] \hat{\psi} = 0, \quad (86)$$

577 where the streamfunction satisfies $\hat{u} = -\partial \hat{\psi} / \partial y$ and $\hat{v} = \partial \hat{\psi} / \partial x$. Applying the boundary condition
 578 $w = 0$ at $z = \pm 1/2$ to the buoyancy equation gives

$$\left[\frac{\partial^2}{\partial t \partial z} + U \frac{\partial^2}{\partial x \partial z} + V \frac{\partial^2}{\partial y \partial z} - B \frac{\partial}{\partial y} \right] \hat{\psi} = 0, \quad (87)$$

579 where the nondimensional buoyancy perturbation is $\hat{b} = \partial \hat{\psi} / \partial z$ using the QG approximation.
 580 From Eqns. 16 and 19 we now write

$$(U, V, N^2) = (-\alpha \gamma B z, \gamma B z, \text{RoPr}_\alpha \gamma B^2), \quad (88)$$

581 and note that N^2 describes the stratification that results from the balance between cross-front ad-
 582 volution and vertical mixing. Eq. 86 has solutions of the form

$$\hat{\psi} = [A \sinh \kappa z + C \cosh \kappa z] e^{ikx+ily+\sigma t}, \quad (89)$$

583 for $\kappa = \sqrt{\text{Ro}N^2(k^2 + l^2)}$ and following Vallis (2006) we Eq. 87 to determine a linear system for
 584 (A, C) . The requirement that the determinant of this system vanishes determines the growth rate,
 585 which can be written

$$\sigma^2 = \frac{B^2}{\kappa^2} \left[\gamma(l - \alpha k) \frac{\kappa}{2} - l \tanh \frac{\kappa}{2} \right] \left[l \coth \frac{\kappa}{2} - \gamma(l - \alpha k) \frac{\kappa}{2} \right]. \quad (90)$$

586 We note that this result reduces to the classical Eady result (Eady 1949) for $\alpha = 0$. Working in our
 587 rotated coordinate system (k', l') , we can show that σ is maximal for $k = -\alpha l$ where

$$\sigma^2 = \frac{\gamma B^2}{\text{Ro}N^2} \left[\frac{\kappa}{2} - \tanh \frac{\kappa}{2} \right] \left[\coth \frac{\kappa}{2} - \frac{\kappa}{2} \right]. \quad (91)$$

588 Therefore, following Eady (1949) and Vallis (2006), we have maximum growth rate

$$\sigma_{max} = \frac{0.31B}{\sqrt{\text{Ro}(1 + \alpha^2)N}}, \quad (92)$$

589 for most unstable wavenumber

$$K_{max} = \frac{1.6}{\sqrt{\text{Ro}N}}. \quad (93)$$

590 Using N^2 from Eq. 88 this result becomes

$$\sigma_{max} = \frac{0.31}{\text{Ro} \sqrt{\text{Pr}_\alpha}}, \quad (94)$$

591 and

$$K_{max} = \frac{1.6 \sqrt{1 + \alpha^2}}{\text{Ro} \sqrt{\text{Pr}_\alpha} B}. \quad (95)$$

592 Therefore the most unstable mode is set by the interaction of edge waves, moderated by the strat-
 593 ification that develops in response to vertical mixing of momentum. Since this stratification is an

594 $O(\text{Ro})$ term in the buoyancy equation, it does not appear in the leading order evolution equations
 595 for b_0 or ψ_0 (equations 47 and 48), and hence its influence on the unstable modes is not captured
 596 by our asymptotic model.

597 The QG predictions for σ_{max} and K_{max} are shown in Figure 11 as functions of α and Ro . Com-
 598 paring these results with Figure 8 we find that they provide reasonably accurate predictions for the
 599 growth rate and wavenumber for $\text{Ro} > 10^{-3}$ where the scale is not set by horizontal diffusion and
 600 the wavenumber of the most unstable mode decreases with increasing Ro . However, the growth
 601 rate from the QG analysis (Eq. 94) is less accurate than the prediction from the asymptotic theory
 602 (Eq. 84) when compared with the numerical simulations. For example, the growth rate in Eq. 94
 603 is independent of α , while the prediction in 84 and the growth rate diagnosed from the simula-
 604 tions decrease with increasing α . This suggests that vertical mixing acts to damp the perturbations
 605 and reduces their growth rate. Nevertheless, the estimate from Eq. 94 still provides a reasonable
 606 approximation to the growth rate.

607 We expect the mixing-induced stratification to limit the size of the most unstable modes when it
 608 would give a smaller value of K_{max} than horizontal diffusion. Using Eq. 83, this occurs when

$$\frac{\text{Ro}B}{\sqrt{48}(1+\alpha^2)\varepsilon^2E} > \frac{1.6\sqrt{1+\alpha^2}}{\text{Ro}\sqrt{\text{Pr}_\alpha}B}. \quad (96)$$

609 Therefore the mixing-induced stratification will be important when

$$\text{Ro} > \frac{3.3(1+\alpha^2)^{3/4}\varepsilon E^{1/2}}{\text{Pr}_\alpha^{1/4}B}. \quad (97)$$

610 For the parameters used in our numerical simulations (specifically $\varepsilon = 0.05$ and $E = 10^{-4}$), this
 611 condition is satisfied for $\text{Ro} \gtrsim 10^{-3}$, consistent with our observations that the fastest growing mode
 612 is not set by horizontal diffusion for this parameter range. We note that using a turbulent Ekman
 613 number scaling of $E \sim u^*/fH$ for turbulent velocity u^* and mixed layer depth H can give values
 614 of E on the order of $10^{-2} - 1$. Therefore in a highly turbulent mixed layer, a diffusive cutoff may

615 be possible for Rossby numbers up to about $\text{Ro} \sim 0.1$. Mathematically, this can help us explain
 616 the apparent inaccuracy of our original prediction for the fastest growing mode. Since a very small
 617 value of $\varepsilon^2 E$ was used in our simulations, the horizontal mixing terms were smaller than any terms
 618 describing the $O(\text{Ro})$ stratification, N^2 , even for small values of Ro . Our theory assumes that these
 619 horizontal mixing terms are dominant and hence we have discrepancies for much smaller values of
 620 Ro than might be anticipated. If we were to instead use a much larger value of E for our numerical
 621 simulations, representative of a turbulent Ekman number, we would find agreement over a much
 622 wider range of Ro as described by Eq. 97. It is also worth re-emphasizing that the lengthscale
 623 used to define Ro is the horizontal domain size in the simulations. Since the most unstable mode
 624 is typically much smaller than the domain size (see Fig. 3), the scale-dependent Rossby number
 625 associated with the size of the most unstable mode will be much larger than Ro .

626 The angle of the most unstable mode from the QG analysis agrees with the theory in §5 and
 627 the simulations. Therefore, we can conclude that the orientation of the most unstable modes are
 628 primarily set by the background flow and is not strongly influenced by the effects of vertical mixing
 629 acting directly on the perturbations.

630 For small K the growth rate from the QG analysis (Eq. 90) becomes

$$\sigma \sim \frac{BK}{\sqrt{12(1+\alpha^2)}Bu}, \quad (98)$$

631 for $Bu = \text{Ro}N^2$. This does not have the same α dependence as Eq. 64, although we note that both
 632 expressions reduce to the classical Eady case for $\alpha = 0$. This discrepancy is likely because the QG
 633 approach does not consider the action of vertical mixing on the perturbations.

634 The analysis of the instability using the QG equations also provides insight into the relative ac-
 635 curacy of growth rate from the analytical theory. In the absence of horizontal mixing, the analytical
 636 theory predicted that the growth rate is a linearly proportional to the horizontal wavenumber (see

Eq. 64). As shown in Eq. 98, the growth rate in the QG analysis also increases linearly with K for small values of K , while stratification decouples the Eady edge waves and suppresses the growth rate for large K . However, the maximum growth rate in the QG analysis is relatively close to the value that would be obtained by using the wavenumber of the fastest growing mode in Eq. 98, which has the same form as the theory in §5. We expect that the true growth rate for the problem admits both a viscous cutoff and a decoupled edge wave cutoff and reduces to the analytical result for small K . If the maximum growth rate in the case of decoupled edge waves is close to the linear, small K region (as is the case in the QG model) then the analytical theory would well describe the growth rate even though it does not capture the cutoff mechanism. This may explain why our growth rate predictions in Figure 10 closely match the numerical simulations.

Note that the Richardson number of this system can be shown to be $Ri = Pr_\alpha$ hence it would be more accurate to use the ageostrophic analysis of Stone (1966). This analysis can be performed using the background state in Eq. 88, although it is much more complicated than the QG analysis. Including non-QG effects reduces the growth rate of the most unstable mode (σ_{max}) by a factor of $\sqrt{1 + Ri}$ and it somewhat reduces the wavenumber of the most unstable mode (K_{max}). Importantly, the dependence of σ_{max} and K_{max} on Ro and α are unchanged by the inclusion of non-QG effects, and hence we use the QG equations here for simplicity.

Recall from figure 3 that modes with $l = \alpha k$ appeared in the simulation with $Ro = 0.1$ which were perpendicular to the anticipated most unstable mode. Setting $l = \alpha k$ in the QG analysis gives

$$\sigma^2 = -\frac{B^2 l^2}{\kappa^2}. \quad (99)$$

These modes are stable and correspond to travelling waves. Therefore, the perpendicular modes observed in Figure 5 do not appear to arise through QG dynamics, and are likely associated with finite Ro effects which we have not considered here.

659 Finally, we note that a similar QG analysis could be carried out for the TTW system with vertical
 660 mixing parameterized using a Laplacian viscosity and diffusivity, as described in Appendix C.
 661 However, in this case Eq. 86 would have to be solved numerically since N^2 depends on z .

662 8. Conclusions and Discussion

663 Here, we examined baroclinic instability in the presence of vertical mixing, where mixing is
 664 parameterized using a simple relaxation towards the local depth average. A theory was developed
 665 which is valid in the limit of small Rossby number, but arbitrary mixing rates. In the limit of no
 666 mixing we recover the long wave limit of baroclinic instability in the Eady model. Vertical mixing
 667 reduces the growth rate and tilts the unstable modes such that they are aligned with the horizontal
 668 velocity, with the angle determined by the relaxation timescale.

669 In the absence of horizontal mixing and a turbulent Prandtl number of 1, the growth rate associ-
 670 ated with the fastest growing modes (from Eq. 61 with $B = 1$) is

$$\sigma = \frac{\text{Ro}}{\alpha(1 + \alpha^2)\text{Bu}}, \quad (100)$$

671 where σ is nondimensionalised by $1/T = HM^2/(fL)$, H is the mixed layer depth, L is a char-
 672 acteristic horizontal length scale, M^2 is the horizontal buoyancy gradient, and f is the Coriolis
 673 parameter. The nondimensional parameters in Eq. 100 are the Rossby number, $\text{Ro} = M^2H/(f^2L)$,
 674 the Burger number, $\text{Bu} = N^2H^2/(f^2L^2)$, where N is the buoyancy frequency associated with a sta-
 675 ble background stratification, and the mixing ratio, $\alpha = \mu/f$, where μ is the vertical mixing rate.

676 Note that the horizontal length scale, L , characterizes the width of the front and not necessarily
 677 the size of the unstable modes. Indeed, Figure 8 shows that the non-dimensional wavenumber of
 678 the most unstable modes is $K \gg 1$ and therefore the scale-dependent Rossby number associated
 679 with the growing perturbations will be significantly larger than Ro.

680 The theoretical growth rate in Eq. 100 decreases with decreasing Ro (e.g. for weak horizon-
 681 tal buoyancy gradients) and decreases with increasing vertical mixing rate. In the absence of a
 682 background stratification ($Bu = 0$) the growth rate is unbounded. However, when a horizontal
 683 Laplacian viscosity and diffusivity is included to parameterize horizontal mixing, the growth rate
 684 is bounded and equal to

$$\sigma = \frac{Ro}{12(1+\alpha^2)^2 \left[\sqrt{\varepsilon^2 E} + \sqrt{\varepsilon^2 E + \frac{\alpha Bu}{12(1+\alpha^2)}} \right]^2}, \quad (101)$$

685 where $E = v/(fH^2)$ is the Ekman number, v is the horizontal viscosity (equal to the diffusivity
 686 since the Prandtl number is assumed to be 1) and H is the mixed layer depth.

687 The theory developed here is valid for asymptotically small Rossby numbers (although the ver-
 688 tical mixing rate can be large). To test the range of validity of the theory, we conducted a series
 689 of numerical simulations. The growth rate and wavenumbers predicted by the theory match those
 690 diagnosed from the simulations very closely for small Rossby numbers. The predicted growth
 691 rate matches the simulations for Rossby numbers up to $O(0.1)$. However for $Ro > O(10^{-3})$, the
 692 most unstable modes in the simulations are significantly larger than those predicted from the the-
 693 ory. This implies that in this range of Ro, the neglected higher order terms become important and
 694 provide a scale selecting mechanism.

695 To investigate this further, we used the quasi-geostrophic (QG) equations to analyze the stability
 696 of a depth-dependent basic state. Here the density of the basic state was set through a balance
 697 between cross-front advection and vertical mixing. Since the stratification that results from this
 698 balance appears at $O(Ro)$ it was not included in the theory described earlier. We also neglected
 699 the direct influence of vertical mixing on the perturbations when applying the QG equations. Re-
 700 sults from the QG analysis show that the horizontal orientation of the fastest growing modes is
 701 largely inherited from the orientation of the background flow. The QG analysis also shows that the

stratification that develops from the cross-front flow can decouple the Eady edge waves, thereby
 providing a high wavenumber cutoff. Although this effect was not included in the theory presented
 in §5, the growth rate predicted from our theory agrees well with the growth rate diagnosed from
 the numerical simulations, even in parts of parameter space where the most unstable wavenumber
 is not set by a viscous cutoff.

Motivated by this, we can combine the predicted growth rate from our theory with the high
 wavenumber cutoff from the QG analysis. To put the results in the context of typical ocean con-
 ditions, it is useful to normalize the growth rate by f and write it as a function of $|\nabla b|/f^2$, which
 has the effect of eliminating the dependence of the growth rate on the aspect ratio. In the case
 with $Bu = 0$, $Pr_E = 1$, and a non-dimensional horizontal buoyancy gradient $B = 1$, the growth rate
 given in Eq. 84 can be written

$$\frac{\sigma}{f} = \frac{KRo}{\sqrt{12(1 + \alpha^2)}} - \frac{f^4}{|\nabla b|^2} E K^2 Ro^2. \quad (102)$$

When the size of the most unstable mode is limited by horizontal mixing,

$$KRo = \frac{|\nabla b|^2}{\sqrt{48f^4(1 + \alpha^2)E}}, \quad (103)$$

and when it is limited by the influence of mixing-induced stratification on the interaction between
 Eady edge waves,

$$KRo = 1.6\sqrt{1 + \alpha^2}. \quad (104)$$

When vertical and horizontal mixing are described using the same characteristic turbulent velocity
 u_* and length scale, l , we have $\alpha \sim E \sim u_*/(fl)$ (see Eq. 7).

Figure 12 shows the growth rate prediction from Eq. 102 with $E = \alpha$, and KRo set by the
 minimum of Eqns. 103 and 104. The dashed line separates regions where the most unstable mode
 is controlled by horizontal mixing through Eq. 103 (the region below the line) and mixing-induced
 stratification through Eq. 104 (the region above the line). The symbols show typical parameters

722 corresponding to winter and summer conditions based on the observations reported in Thompson
723 et al. (2016). In the winter when submesoscale activity was clearly observed, the size of the most
724 unstable mode is limited by mixing-induced stratification and the growth rate from Eq. 102 is close
725 to the inviscid prediction from Stone (1966). However, for parameters more typical of conditions
726 during summer, Figure 12 suggests that mixing associated with small-scale turbulence can limit
727 the size and dramatically reduce the growth rate of the unstable modes. This result might help
728 explain the apparent absence of submesoscale activity in the summer months.

729 For the inviscid Eady problem (here with $\alpha = 0$), the dominant source of energy for the growing
730 baroclinic modes is the buoyancy flux. Here, we find that for relatively large mixing rates, the
731 dominant energy balance is between the buoyancy flux and the dissipation associated with ver-
732 tical mixing, with the small residual corresponding to the kinetic energy growth. Therefore the
733 instability is driven by a transfer of potential energy to the growing perturbations, consistent with
734 baroclinic instability, although now most of the energy is dissipated by vertical mixing, which acts
735 to reduce the growth rate of the unstable modes.

736 For larger values of α and Ro , the numerical simulations show evidence of small scale modes
737 with $l = \alpha k$ that are perpendicular to the predicted direction. These might be associated with the
738 skew flux term in the leading order buoyancy equation (Eq. 27) which cannot be neglected for large
739 Ro and acts to destabilize modes with $l = \alpha k$. The energy budget suggests that these modes have
740 a different energy source involving both the buoyancy flux and the shear production. These modes
741 have not been studied in detail here since our theory is not valid for this range of parameters.

742 As noted above, the growth rate of the most unstable mode predicted from our theory matches the
743 numerical simulations up to a Rossby number of about 0.1. This range includes many open ocean
744 fronts. For example, based on a year-long timeseries from the OSMOSIS campaign, Thompson
745 et al. (2016) found that the strongest fronts observed had $|\nabla b| \sim 10^{-7} \text{s}^{-2}$. For mixed layer depths

746 in the range 20 – 200m and a horizontal scale between 20km, this corresponds to a Rossby number
747 ranging from 0.01 – 0.1. Stronger and/or sharper fronts such as the Gulf Stream (Thomas et al.
748 2013) are likely to be strongly influenced by the relatively large Rossby numbers characterizing
749 these fronts, and our results might not be applicable.

750 The turbulent thermal wind (TTW) model considered in Wenegrat and McPhaden (2016);
751 McWilliams (2016); Crowe and Taylor (2018) used a large turbulent Ekman number instead of
752 relaxation to represent mixed layer turbulence. As shown in Appendix C, the TTW model is also
753 susceptible to the instability described here, and we expect that any turbulence parametrization in
754 which the leading order velocity is linear in the buoyancy gradient will exhibit the same instability.

755 We have approached the stability problem by seeking analytical solutions to the asymptotic
756 equations which are valid for small Rossby numbers. Another approach would be to solve the
757 linearized equations numerically, without making any assumptions about the size of the Rossby
758 number. This could be viewed as an extension to Stone (1970) and Stamper and Taylor (2017) with
759 the addition of vertical mixing. This would permit non-geostrophic processes such as symmetric
760 instability which are not included in the limit of small Ro.

761 Here, we have assumed that the relaxation ratio, α is constant which effectively prescribes the
762 vertical mixing rate. This allows us to isolate and study the influence of vertical mixing on mixed
763 layer instabilities, but the assumption of constant α does not allow the instabilities to modify the
764 vertical mixing rate. Previous studies (e.g. Taylor and Ferrari 2011; Taylor 2016) have found that
765 the stable stratification induced by baroclinic and symmetric instability significantly reduces the
766 rate of vertical mixing. We speculate that a reduction in α would enhance the growth rate of the
767 unstable modes, providing a positive feedback mechanism. This hypothesis could be tested in
768 future work.

769 *Acknowledgments.* The authors are grateful to two anonymous referees for constructive com-
770 ments. The authors would also like to thank Jörn Callies, Raffaele Ferrari, Leif Thomas, and
771 Jacob Wenegrat for stimulating and helpful conversations. We are particularly grateful to Bill
772 Young for very helpful discussions and for comments on a draft of the paper.

773 APPENDIX A

774 Transient Solution

775 In §3 we calculated the asymptotic solution for \mathbf{u}_0 , b_0 and b'_1 for the long time evolution. Here we
776 include the transient evolution on the timescale τ for an initial flow with arbitrary vertical structure
777 (e.g. thermal wind flow). Again the leading order buoyancy is assumed to be depth independent but
778 we allow the buoyancy deviation, b'_1 , to have arbitrary initial vertical structure. This setup allows
779 us to initialize the flow in thermal wind balance with a depth independent buoyancy, the transient
780 evolution causes the front to slump over and the velocity to develop a cross-front component.

781 a. Order 1 Equations

782 The leading order buoyancy balance is

$$\frac{\partial b_0}{\partial \tau} + \frac{\alpha}{\text{Pr}_\alpha} b'_0 = 0, \quad (\text{A1})$$

783 so we take solution with b_0 to be depth independent and hence independent of τ , therefore $b_0 =$
784 $b_0(x, y, t)$.

⁷⁸⁵ The leading order velocity balance is given by

$$\frac{\partial u_0}{\partial \tau} - v_0 = -\frac{\partial p_0}{\partial x} - \alpha u'_0, \quad (\text{A2a})$$

$$\frac{\partial v_0}{\partial \tau} + u_0 = -\frac{\partial p_0}{\partial y} - \alpha v'_0, \quad (\text{A2b})$$

$$0 = -\frac{\partial p_0}{\partial z} + b_0, \quad (\text{A2c})$$

$$\frac{\partial u_0}{\partial x} + \frac{\partial v_0}{\partial y} + \frac{\partial w_0}{\partial z} = 0, \quad (\text{A2d})$$

⁷⁸⁶ hence the pressure can be written as

$$p_0 = z b_0 + \bar{p}_0, \quad (\text{A3})$$

⁷⁸⁷ and the horizontal momentum equations and mass conservation equation can be depth averaged to
⁷⁸⁸ give

$$\frac{\partial \bar{u}_0}{\partial \tau} - \bar{v}_0 = -\frac{\partial \bar{p}_0}{\partial x}, \quad (\text{A4a})$$

$$\frac{\partial \bar{v}_0}{\partial \tau} + \bar{u}_0 = -\frac{\partial \bar{p}_0}{\partial y}, \quad (\text{A4b})$$

$$\frac{\partial \bar{u}_0}{\partial x} + \frac{\partial \bar{v}_0}{\partial y} = 0. \quad (\text{A4c})$$

⁷⁸⁹ Subtracting the depth-averaged horizontal momentum equations from equations A2 gives evolution
⁷⁹⁰ equations for the horizontal velocity perturbations and vertical velocity

$$\left[\frac{\partial}{\partial \tau} + \alpha \right] u'_0 - v'_0 = -z \frac{\partial b_0}{\partial x}, \quad (\text{A5a})$$

$$\left[\frac{\partial}{\partial \tau} + \alpha \right] v'_0 + u'_0 = -z \frac{\partial b_0}{\partial y}, \quad (\text{A5b})$$

$$\frac{\partial u'_0}{\partial x} + \frac{\partial v'_0}{\partial y} + \frac{\partial w_0}{\partial z} = 0. \quad (\text{A5c})$$

⁷⁹¹ Equations A5 can be solved to get

$$\mathbf{u}'_{H0} = A_1(z, \tau) \nabla_H b_0 + A_2(z, \tau) \mathbf{k} \times \nabla_H b_0, \quad (\text{A6})$$

⁷⁹² and

$$w_0 = A_3(z, \tau) \nabla_H^2 b_0. \quad (\text{A7})$$

⁷⁹³ where

$$A_1 = \frac{-\alpha z}{1 + \alpha^2} + \left[A_1^0(z) + \frac{\alpha z}{1 + \alpha^2} \right] e^{-\alpha \tau} \cos \tau + \left[A_2^0(z) - \frac{z}{1 + \alpha^2} \right] e^{-\alpha \tau} \sin \tau, \quad (\text{A8a})$$

$$A_2 = \frac{z}{1 + \alpha^2} + \left[A_2^0(z) - \frac{z}{1 + \alpha^2} \right] e^{-\alpha \tau} \cos \tau - \left[A_1^0(z) + \frac{\alpha z}{1 + \alpha^2} \right] e^{-\alpha \tau} \sin \tau, \quad (\text{A8b})$$

$$A_3 = \frac{\alpha(z^2 - \frac{1}{4})}{2(1 + \alpha^2)} - e^{-\alpha \tau} \cos \tau \int_{-1/2}^z A_1^0(z') dz' + \frac{\alpha z'}{1 + \alpha^2} dz' - e^{-\alpha \tau} \sin \tau \int_{-1/2}^z A_2^0(z') dz' - \frac{z'}{1 + \alpha^2} dz', \quad (\text{A8c})$$

⁷⁹⁴ where (A_1^0, A_2^0) describes the initial horizontal flow. Once the transients have decayed the balanced
⁷⁹⁵ solutions are

$$\mathbf{u}'_{H0} = \gamma [-\alpha \nabla_H b_0 + \mathbf{k} \times \nabla_H b_0] z, \quad (\text{A9})$$

⁷⁹⁶ and

$$w_0 = \frac{\alpha \gamma (4z^2 - 1)}{8} \nabla_H^2 b_0, \quad (\text{A10})$$

⁷⁹⁷ for $\gamma = 1/(1 + \alpha^2)$. From the depth-averaged mass conservation equation we can write

$$\bar{\mathbf{u}}_{H0} = -\nabla \times (\psi_0 \mathbf{k}), \quad (\text{A11})$$

⁷⁹⁸ for streamfunction $\psi_0 = \bar{p}_0$. Hence

$$\mathbf{u}_{H0} = -\nabla \times (\psi_0 \mathbf{k}) + A_1(z, \tau) \nabla_H b_0 + A_2(z, \tau) \mathbf{k} \times \nabla_H b_0. \quad (\text{A12})$$

⁷⁹⁹ b. Order Ro Equations

⁸⁰⁰ The $O(\text{Ro})$ buoyancy equation is

$$\frac{\partial b_1}{\partial \tau} + \frac{\partial b_0}{\partial t} + \mathbf{u}_{H0} \cdot \nabla_H b_0 + \mathcal{N}^2 w_0 = -\frac{\alpha}{\text{Pr}_\alpha} b'_1, \quad (\text{A13})$$

801 and subtracting the depth average gives

$$\left[\frac{\partial}{\partial \tau} + \frac{\alpha}{\text{Pr}_\alpha} \right] b'_1 = -\mathbf{u}'_{H0} \cdot \nabla_H b_0 - \mathcal{N}^2 w'_0. \quad (\text{A14})$$

802 When $\mathcal{N}^2 = 0$ the general solution is given by

$$b'_1 = A_4(z, \tau) |\nabla_H b_0|^2, \quad (\text{A15})$$

803 where

$$A_4 = \frac{\text{Pr}_\alpha z}{1 + \alpha^2} + \left[A_4^0(z) - \frac{\text{Pr}_\alpha z}{1 + \alpha^2} + \frac{\left[A_1^0(z) + \frac{\alpha z}{1 + \alpha^2} \right] \alpha \left(1 - \frac{1}{\text{Pr}_\alpha} \right) + \left[A_2^0(z) - \frac{z}{1 + \alpha^2} \right]}{1 + \alpha^2 \left(1 - \frac{1}{\text{Pr}_\alpha} \right)^2} \right] e^{-\frac{\alpha}{\text{Pr}_\alpha} \tau} \\ + \left[\frac{\left[A_1^0(z) + \frac{\alpha z}{1 + \alpha^2} \right] \left(\sin \tau - \alpha \left(1 - \frac{1}{\text{Pr}_\alpha} \right) \cos \tau \right) - \left[A_2^0(z) - \frac{z}{1 + \alpha^2} \right] \left(\cos \tau + \alpha \left(1 - \frac{1}{\text{Pr}_\alpha} \right) \sin \tau \right)}{1 + \alpha^2 \left(1 - \frac{1}{\text{Pr}_\alpha} \right)^2} \right] e^{-\alpha \tau}, \quad (\text{A16})$$

804 for initial vertical structure described by $A_4^0(z)$. The general steady state solution is given by

$$b'_1 = \text{Pr}_\alpha \gamma \left[z |\nabla_H b_0|^2 - \mathcal{N}^2 \frac{12z^2 - 1}{24} \nabla_H^2 b_0 \right], \quad (\text{A17})$$

805 and calculating \bar{b}_1 requires the $O(\text{Ro}^2)$ buoyancy equation.

806

APPENDIX B

807

Analytic Solution with Relaxation and Diffusion

808 If we include vertical diffusion in the leading order velocity balance by taking $E = O(1)$, we can

809 obtain the solution

$$\mathbf{u}'_{H0} = -\sqrt{E} [B_1 \nabla_H b_0 + B_2 \mathbf{k} \times \nabla_H b_0], \quad (\text{B1})$$

810 where

$$B_1 = \alpha \zeta / (1 + \alpha^2) + i C_1 \sinh[\sqrt{\alpha + i} \zeta] - i C_2 \sinh[\sqrt{\alpha - i} \zeta], \quad (\text{B2a})$$

$$B_2 = -\zeta / (1 + \alpha^2) + C_1 \sinh[\sqrt{\alpha + i} \zeta] + C_2 \sinh[\sqrt{\alpha - i} \zeta], \quad (\text{B2b})$$

⁸¹¹ and

$$\zeta = z/\sqrt{E}. \quad (\text{B3})$$

⁸¹² Using boundary conditions of no vertical shear on the top and bottom surfaces gives that

$$\begin{bmatrix} i\sqrt{\alpha+i}\cosh\left[\sqrt{\frac{\alpha+i}{4E}}\right] & -i\sqrt{\alpha-i}\cosh\left[\sqrt{\frac{\alpha-i}{4E}}\right] \\ \sqrt{\alpha+i}\cosh\left[\sqrt{\frac{\alpha+i}{4E}}\right] & \sqrt{\alpha-i}\cosh\left[\sqrt{\frac{\alpha-i}{4E}}\right] \end{bmatrix} \begin{bmatrix} C_1 \\ C_2 \end{bmatrix} = \frac{1}{1+\alpha^2} \begin{bmatrix} -\alpha \\ 1 \end{bmatrix}, \quad (\text{B4})$$

⁸¹³ which can be inverted to obtain solution

$$\begin{bmatrix} C_1 \\ C_2 \end{bmatrix} = \frac{1}{2(1+\alpha^2)} \begin{bmatrix} \frac{1+\alpha i}{\sqrt{\alpha+i}\cosh\zeta_{\alpha+}} \\ \frac{1-\alpha i}{\sqrt{\alpha-i}\cosh\zeta_{\alpha-}} \end{bmatrix}, \quad (\text{B5})$$

⁸¹⁴ for

$$\zeta_{\alpha\pm} = \sqrt{\frac{\alpha \pm i}{4E}} = \sqrt{\alpha \pm i} \zeta_0, \quad (\text{B6})$$

⁸¹⁵ and $\sqrt{*}$ denoting the principle value of the square root with branch cut taken along the line $z \in$
⁸¹⁶ $-\mathbb{R}_0^+$. The leading order vertical velocity can be obtained by integrating the mass conservation
⁸¹⁷ equation as before which gives solution

$$w_0 = E \left[\frac{\alpha^2 - 1}{(\alpha^2 + 1)^2} + \frac{\alpha(\zeta^2 - \zeta_0^2)}{2(1 + \alpha^2)} + \frac{iC_1}{\sqrt{\alpha+i}} \cosh[\sqrt{\alpha+i}\zeta] - \frac{iC_2}{\sqrt{\alpha-i}} \cosh[\sqrt{\alpha-i}\zeta] \right] \nabla_H^2 b_0, \quad (\text{B7})$$

⁸¹⁸ for $\zeta_0 = 1/2\sqrt{E}$.

⁸¹⁹ We can now use this leading order solution for the velocity to calculate the $O(\text{Ro})$ solution for
⁸²⁰ the buoyancy perturbation, the governing equation is

$$\mathbf{u}'_{H0} \cdot \nabla_H b_0 = \frac{E}{\text{Pr}} \frac{\partial^2 b'_1}{\partial z^2} - \frac{\alpha}{\text{Pr}} b'_1, \quad (\text{B8})$$

⁸²¹ hence

$$\left[\frac{\partial^2}{\partial \zeta^2} - \alpha \right] b'_1 = -\sqrt{E} \text{Pr} B_1 |\nabla_H b_0|^2, \quad (\text{B9})$$

⁸²² which has solution

$$b'_1 = -\sqrt{E} \text{Pr} B_2 |\nabla_H b_0|^2. \quad (\text{B10})$$

823 For small E this solution reduces to the solution given above in the region away from the bound-
 824 aries. We use this solution to initialize the numerical simulations so that the initial state matches
 825 the no stress boundary conditions and hence will not produce inertial waves while adjusting to a
 826 balanced state.

APPENDIX C

Instability in the viscous TTW model

827 In this section, we analyze the stability of the the Turbulent Thermal Wind (TTW) model used
 828 in Crowe and Taylor (2018) where vertical mixing is parameterized by a Laplacian viscosity and
 829 diffusivity. We also include a background streamfunction, ψ_0 . The Steady state solution is

$$\mathbf{u}_H = -\nabla \times (\psi_0 \mathbf{k}) - \sqrt{E} (K_0'' \nabla_H b_0 + K_0 \mathbf{k} \times \nabla_H b_0) + O(\text{Ro}), \quad (\text{C1})$$

$$w = E K_0' \nabla_H^2 b_0 + O(\text{Ro}), \quad (\text{C2})$$

830 and

$$b = b_0 - \text{RoPr} \sqrt{E} K_0 |\nabla_H b_0|^2 + O(\text{Ro}^2), \quad (\text{C3})$$

831 where K_0 and its derivatives are given in Crowe and Taylor (2018). Note that this model does not
 832 include a stratification so $Bu = 0$ and we are using an order 1 Ekman number to describe the effects
 833 of turbulence. Here we have used a constant vertical turbulent viscosity and diffusivity profile, this
 834 is just for convenience and the resulting equations will be similar for arbitrary vertical profiles.

835 Using the depth-averaged buoyancy and vorticity equations, equations 23 and 40, and includ-
 836 ing horizontal diffusion we can write the governing equations for the background buoyancy and
 837 streamfunction as

$$\frac{\partial b_0}{\partial t} + J(\psi_0, b_0) = \frac{\varepsilon^2 E}{\text{RoPr}} \nabla_H^2 b_0, \quad (\text{C4})$$

841 and

$$\frac{\partial \nabla_H^2 \psi_0}{\partial t} + J(\psi_0, \nabla_H^2 \psi_0) - \frac{\epsilon^2 E}{Ro} \nabla_H^4 \psi_0 = \\ E \nabla_H \cdot \left[\left(2\bar{K}_0'^2 \nabla_H b_0 + \left[\bar{K}_0'^2 - \bar{K}_0^2 \right] \mathbf{k} \times \nabla_H b_0 \right) \nabla_H^2 b_0 \right]. \quad (C5)$$

842 Note that the right hand side of Eq. C4 can be related to the diabatic PV flux (Thomas 2005;
 843 Wenegrat et al. 2018). These equations are of the same form as the governing equations for the
 844 relaxation model considered above hence we expect instabilities with the corresponding growth
 845 rate

$$\sigma_{\pm} = -\frac{\epsilon^2 E}{2Ro} \left[1 + \frac{1}{Pr} \right] (k^2 + l^2) \pm \\ \sqrt{\left[\frac{1}{Pr} - 1 \right]^2 \frac{\epsilon^4 E^2}{4Ro^2} (k^2 + l^2)^2 - EB^2 \left[2\bar{K}_0'^2 kl + (\bar{K}_0'^2 - \bar{K}_0^2) l^2 \right]}, \quad (C6)$$

846 for frontal gradient B and horizontal wavevector (k, l) . In the case $Pr = 1$ this simplifies to

$$\sigma_{\pm} = -\frac{\epsilon^2 E}{Ro} (k^2 + l^2) \pm \sqrt{-EB^2 \left[2\bar{K}_0'^2 kl + (\bar{K}_0'^2 - \bar{K}_0^2) l^2 \right]}. \quad (C7)$$

847 The last term in square brackets in equations C6 and C7 is a symmetric quadratic form so can be
 848 diagonalized by an orthogonal transformation. Therefore the fastest growing modes for a given
 849 wavenumber will be tilted with angle dependent only on a function of the Ekman number. The
 850 fastest growing mode for a given wavenumber, $K = \sqrt{k^2 + l^2}$, is

$$\sigma_{\pm} = -\frac{\epsilon^2 E}{2Ro} \left[1 + \frac{1}{Pr} \right] K^2 + \sqrt{\left[\frac{1}{Pr} - 1 \right]^2 \frac{\epsilon^4 E^2}{4Ro^2} K^4 + \lambda EB^2 K^2}, \quad (C8)$$

851 for eigenvalue

$$\lambda = -\frac{1}{2} \left[\bar{K}_0'^2 - \bar{K}_0^2 - \sqrt{4\bar{K}_0'^2 + (\bar{K}_0'^2 - \bar{K}_0^2)^2} \right], \quad (C9)$$

852 with angle

$$\theta = \arctan \left[\frac{\bar{K}_0'^2 - \bar{K}_0^2 + \sqrt{4\bar{K}_0'^2 + (\bar{K}_0'^2 - \bar{K}_0^2)^2}}{2\bar{K}_0'^2} \right], \quad (C10)$$

853 from the down-front direction.

854 In the case $\text{Pr} = 1$ the maximum growth rate reduces to

$$\sigma_{max} = \sqrt{\lambda E} BK - \frac{\varepsilon^2 E K^2}{\text{Ro}}, \quad (\text{C11})$$

855 which is the analogous result to Eq. 84 and has fastest growing mode

$$K_{max} = \frac{\sqrt{\lambda} B \text{Ro}}{2\varepsilon^2 \sqrt{E}}, \quad (\text{C12})$$

856 with corresponding growth rate

$$\sigma(K_{max}) = \frac{\lambda B^2 \text{Ro}}{4\varepsilon^2}. \quad (\text{C13})$$

857 Figure C1 shows the formation of baroclinic instability for $\alpha = 0$, $E = 0.1$ and $\text{Ro} = 0.01$. We
858 can see that the evolution and structure of the instability is similar to the case of the relaxation
859 parametrisation with modes tilted by the angled TTW flow.

860 References

- 861 Bachman, S. D., and J. R. Taylor, 2016: Numerical simulations of the equilibrium between eddy-
862 induced restratification and vertical mixing. *Journal of Physical Oceanography*, **46** (3), 919–
863 935.
- 864 Boccaletti, G., R. Ferrari, and B. Fox-Kemper, 2007: Mixed layer instabilities and restratification.
865 *Journal of Physical Oceanography*, **37** (9), 2228–2250.
- 866 Callies, J., and R. Ferrari, 2013: Interpreting energy and tracer spectra of upper-ocean turbulence
867 in the submesoscale range (1–200 km). *Journal of Physical Oceanography*, **43** (11), 2456–2474.
- 868 Callies, J., and R. Ferrari, 2018: Baroclinic instability in the presence of convection. *Journal of
869 Physical Oceanography*, **48** (1), 45–60.

- 870 Callies, J., R. Ferrari, J. M. Klymak, and J. Gula, 2015: Seasonality in submesoscale turbulence.
871 *Nature communications*, **6**, 6862.
- 872 Callies, J., G. Flierl, R. Ferrari, and B. Fox-Kemper, 2016: The role of mixed-layer instabilities in
873 submesoscale turbulence. *J. Fluid Mech.*, **788**, 5–41.
- 874 Capet, X., E. Campos, and A. Paiva, 2008: Submesoscale activity over the argentinian shelf.
875 *Geophysical Research Letters*, **35 (15)**.
- 876 Charney, J. G., 1973: *Planetary Fluid Dynamics*, chap. Symmetric Circulations in Idealized Mod-
877 els, 128–141. D. Reidel Publishing Company.
- 878 Crowe, M. N., and J. R. Taylor, 2018: The evolution of a front in turbulent thermal wind balance,
879 part 1: Theory. *J. Fluid Mech.*, **850**, 179–211.
- 880 Crowe, M. N., and J. R. Taylor, 2019: The evolution of a front in turbulent thermal wind balance,
881 part 2: Numerical simulations. *J. Fluid Mech.*, **in press**.
- 882 Eady, E. T., 1949: Long waves and cyclone waves. *Tellus*, **1**, 33–52.
- 883 Ferrari, R., and W. R. Young, 1997: On the development of thermohaline correlations as a result
884 of nonlinear diffusive parameterizations. *J. Mar. Res.*, **55**, 1069–1101.
- 885 Fox-Kemper, B., R. Ferrari, and R. Hallberg, 2008: Parameterization of mixed layer eddies. part
886 i: Theory and diagnosis. *Journal of Physical Oceanography*, **38 (6)**, 1145–1165.
- 887 Gula, J., M. J. Molemaker, and J. C. McWilliams, 2014: Submesoscale cold filaments in the gulf
888 stream. *J. Phys. Oceanogr.*, **44**, 2617–2643.
- 889 Kato, H., and O. M. Phillips, 1969: On the penetration of a turbulent layer into stratified fluid. *J.*
890 *Fluid Mech.*, **37**, 643–655.

- 891 Lorbacher, K., D. Dommelget, P. Niiler, and A. Köhl, 2006: Ocean mixed layer depth: A
892 subsurface proxy of ocean-atmosphere variability. *Journal of Geophysical Research: Oceans*,
893 **111** (C7).
- 894 Mahadevan, A., E. D'asaro, C. Lee, and M. J. Perry, 2012: Eddy-driven stratification initiates
895 north atlantic spring phytoplankton blooms. *Science*, **337** (6090), 54–58.
- 896 McWilliams, J. C., 2016: Submesoscale surface fronts and filaments: Secondary circulation, buoy-
897 ancy flux, and frontogenesis. *unpublished*.
- 898 Mensa, J. A., Z. Garraffo, A. Griffa, T. M. Özgökmen, A. Haza, and M. Veneziani, 2013: Sea-
899 sonality of the submesoscale dynamics in the gulf stream region. *Ocean Dynamics*, **63** (8),
900 923–941.
- 901 Rudnick, D. L., and R. Ferrari, 1999: Compensation of horizontal temperature and salinity gradi-
902 ents in the ocean mixed layer. *Science*, **283** (5401), 526–529.
- 903 Sasaki, H., P. Klein, B. Qiu, and Y. Sasai, 2014: Impact of oceanic-scale interactions on
904 the seasonal modulation of ocean dynamics by the atmosphere. *Nature communications*, **5**,
905 ncomms6636.
- 906 Schumann, U., and T. Gerz, 1995: Turbulent mixing in stably stratified shear flows. *Journal of*
907 *Applied Meteorology*, **34** (1), 33–48.
- 908 Shakespeare, C. J., and J. Taylor, 2013: A generalized mathematical model of geostrophic adjust-
909 ment and frontogenesis: uniform potential vorticity. *J. Fluid Mech.*, **736**, 366–413.
- 910 Shay, T. J., and M. C. Gregg, 1986: Convectively driven turbulent mixing in the upper ocean. *J.*
911 *Phys. Oceanogr.*, **16**, 1777–1798.

- 912 Stamper, M. A., and J. R. Taylor, 2017: The transition from symmetric to baroclinic instability in
913 the eady model. *Ocean Dynamics*, **67** (1), 65–80.
- 914 Stone, P. H., 1966: On non-geostrophic baroclinic stability. *J. Atmos. Sci.*, **23**, 390–400.
- 915 Stone, P. H., 1970: On non-geostrophic baroclinic stability: Part ii. *Journal of the Atmospheric*
916 *Sciences*, **27** (5), 721–726.
- 917 Sverdrup, H., 1953: On vernal blooming of phytoplankton. *Conseil Exp. Mer*, **18**, 287–295.
- 918 Tandon, A., and C. Garrett, 1994: Mixed layer restratification due to a horizontal density gradient.
919 *J. Phys. Oceanogr.*, **24** (6), 1419–1424.
- 920 Taylor, G. I., 1953: Dispersion of soluble matter in solvent flowing slowly through a tube. *Proc.*
921 *Roy. Soc. A.*, **219**, 186–203.
- 922 Taylor, J. R., 2008: Numerical simulations of the stratified oceanic bottom boundary layer. Ph.D.
923 thesis, University of California, San Diego.
- 924 Taylor, J. R., 2016: The influence of submesoscale restratification and convection on light-limited
925 phytoplankton growth. *Geophys. Res. Lett.*, 2016GL069106.
- 926 Taylor, J. R., and R. Ferrari, 2011: Numerical simulations of the competition between wind-driven
927 mixing and surface heating in triggering spring phytoplankton blooms. *Limnol. Oceanogr.*,
928 **56** (6), 2293–2307.
- 929 Thomas, L. N., 2005: Destruction of potential vorticity by winds. *J. Phys. Oceanogr.*, **35**, 2457–
930 2466.
- 931 Thomas, L. N., J. R. Taylor, R. Ferrari, and T. M. Joyce, 2013: Symmetric instability in the gulf
932 stream. *Deep Sea Research Part II: Topical Studies in Oceanography*, **91**, 96–110.

- 933 Thompson, A. F., A. Lazar, C. Buckingham, A. C. Naveira Garabato, G. M. Damerell, and K. J.
934 Heywood, 2016: Open-ocean submesoscale motions: A full seasonal cycle of mixed layer in-
935 stabilities from gliders. *J. Phys. Oceanogr.*, **46** (4), 1285–1307.
- 936 Thorpe, S. A., 2005: *The turbulent ocean*. Cambridge University Press.
- 937 Vallis, G. K., 2006: *Atmospheric and Oceanic Fluid Dynamics*. Cambridge University Press.
- 938 Venayagamoorthy, S. K., and D. D. Stretch, 2010: On the turbulent prandtl number in homoge-
939 neous stably stratified turbulence. *Journal of Fluid Mechanics*, **644**, 359–369.
- 940 Wenegrat, J., L. N. Thomas, J. Gula, and J. C. McWilliams, 2018: Effects of the submesoscale on
941 the potential vorticity budget of ocean mode waters. *J. Phys. Oceanogr.*, **48**, 2141–2165.
- 942 Wenegrat, J. O., and M. J. McPhaden, 2016: A simple analytical model of the diurnal ekman layer.
943 *J. Phys. Oceanogr.*, **46** (9), 2877–2894.
- 944 Young, W. R., 1994: The subinertial mixed layer approximation. *J. Phys. Oceanogr.*, **24**, 1812–
945 1826.
- 946 Young, W. R., and L. Chen, 1995: Baroclinic instability and thermohaline gradient alignment in
947 the mixed layer. *J. Phys. Oceanogr.*, **25**, 3172–3185.
- 948 Young, W. R., P. B. Rhines, and C. J. R. Garrett, 1982: Shear-flow dispersion, internal waves and
949 horizontal mixing in the ocean. *J. Phys. Oceanogr.*, **12**, 515–527.

Parameter	Symbol	Definition
Rossby Number	Ro	$\varepsilon \Delta b / f^2 L$
Relaxation Ratio	α	μ_u / f
Prandtl Number (α)	Pr_α	μ_u / μ_b
Aspect Ratio	ε	H / L
Burger Number	Bu	$N^2 H^2 / f^2 L^2$

TABLE 1: Definitions of the dimensionless parameters and their values for buoyancy difference, Δb , Coriolis parameter, f , background stratification, N^2 , horizontal lengthscale, L , vertical lengthscale, H , and momentum and buoyancy relaxation rates, μ_u and μ_b .

Parameter	Symbol	Mahadevan et al. (N. Atl., spring)	Thompson et al. (N. Atl., summer)	Thompson et al. (N. Atl., winter)	Thomas et al. (Gulf Stream, winter)
Mixed layer depth	H (m)	300	20	200	100
Coriolis parameter	f (s ⁻¹)	1.3×10^{-4}	1.1×10^{-4}	1.1×10^{-4}	9.0×10^{-5}
Horiz. buoyancy grad.	$ \nabla b $ (s ⁻²)	7×10^{-9}	10^{-8}	10^{-7}	10^{-7}
Horizontal scale	L (km)	300	5	15	10
Turbulent velocity	u_* (m s ⁻¹)	10^{-2}	10^{-2}	2×10^{-2}	2×10^{-2}
Aspect ratio	ϵ	10^{-3}	4×10^{-3}	10^{-2}	10^{-2}
Rossby number	$\text{Ro} = \frac{ \nabla b }{f^2} \epsilon$	10^{-3}	4×10^{-3}	0.1	0.5
Relaxation ratio	$\alpha = \frac{u_*}{fH}$	0.3	5	1	1

TABLE 2: Estimates of physical scales and nondimensional parameters for three open ocean fronts as estimated based on observations reported in Mahadevan et al. (2012); Thompson et al. (2016); Thomas et al. (2013).

958 LIST OF FIGURES

- 959 **Fig. 1.** Real and imaginary parts of the growth rate σ_{\pm} , predicted from the theory for $\mathcal{E} = \mathcal{D} = 0$
 960 and $\mathcal{B}^2 = 0.213$ corresponding to $\alpha = 0.5$ and $B = 2$. The black lines are $k = -\alpha l$ and the
 961 white lines are $l = \alpha k$. Note that the top and bottom rows have different color bars. 60
- 962 **Fig. 2.** The real and imaginary parts of the growth rate, σ_{\pm} , predicted from the theory for $\mathcal{E} = \mathcal{D} =$
 963 2.5×10^{-3} and $\mathcal{B}^2 = 0.213$ corresponding to $\alpha = 0.5$ and $B = 2$. The black lines are $k = -\alpha l$
 964 and the white lines are $l = \alpha k$ 61
- 965 **Fig. 3.** Depth-averaged buoyancy perturbation, $\bar{b}(x, y) - Bx$ from a nonlinear numerical simulation
 966 with $\text{Ro} = 10^{-3}$ and $\alpha = 0.4$ at several times as indicated. The formation of the linear
 967 instability and the transition to nonlinear instability can be seen. 62
- 968 **Fig. 4.** Depth-averaged buoyancy perturbation, $\bar{b}(x, y) - Bx$ from numerical simulations with $\alpha =$
 969 0.4 and $\alpha = 1$. In both cases $\text{Ro} = 10^{-3}$ and the fields are shown at time $t = 0.314$. The black
 970 lines show the predicted wavevector direction, $k = -\alpha l$, which should be perpendicular to
 971 lines of constant phase. 63
- 972 **Fig. 5.** Depth-averaged buoyancy perturbation, $\bar{b}(x, y) - Bx$ for $\alpha = 0.4$ and several Rossby numbers
 973 during the phase of linear perturbation growth in several numerical simulations. For
 974 $\text{Ro} = 0.1$ growing modes appear which are perpendicular to those predicted by the analyti-
 975 cal theory, indicating a breakdown of the theory due to the relatively large Rossby number.
 976 64
- 977 **Fig. 6.** The magnitude of terms in the volume-averaged energy budget from numerical simulations
 978 for several values of Rossby numbers and α . The terms are as given in Eqs. 77 and 78,
 979 specifically, the shear production is denoted \mathcal{S} , buoyancy flux, \mathcal{F} , and dissipation via vertical
 980 mixing (relaxation), \mathcal{R} . The case of $\alpha = 0$ corresponds to the classical Eady model. 65
- 981 **Fig. 7.** Perturbation growth rate, σ_N , diagnosed from the numerical simulations for a range of
 982 Rossby numbers, Ro and relaxation ratios, α . The dashed lines show the interval of ex-
 983 ponential growth and the average value of σ_N within this region. 66
- 984 **Fig. 8.** Perturbation growth rate, σ_N , and the wavenumber, $K = \sqrt{k^2 + l^2}$, for the fastest growing
 985 mode inferred from the numerical simulations as functions of Ro and α 67
- 986 **Fig. 9.** Amplitudes of the horizontal Fourier coefficients from the depth-averaged buoyancy pertur-
 987 bation, $\bar{b}(x, y) - Bx$, calculated from the numerical simulations for a range of Ro and α . The
 988 line $k = -\alpha l$ is shown in white and the maximum wavenumber, K_{max} , is given by the white
 989 circle. 68
- 990 **Fig. 10.** Perturbation growth rate, σ , diagnosed from the numerical simulations (σ_N) and the maxi-
 991 mum growth rate predicted from the theory (σ_{max}). 69
- 992 **Fig. 11.** Wavenumber and growth rate of the most unstable mode from the QG analysis (Eqs. 94 and
 993 95) as functions of Ro and α 70
- 994 **Fig. 12.** Predicted growth rate of the most unstable modes from Eq. 102 where the wavenumber is set
 995 by the smaller of Eq. 103 and 104. The dashed line separates regions where the wavenumber
 996 is set by Eq. 103 (below the line) from regions where the wavenumber is set by Eq. 104
 997 (above the line). The symbols indicate typical parameters from the OSMOSIS survey as
 998 reported in Thompson et al. (2016) in the winter and summer (see Table 2 for values). 71

999 **Fig. C1.** The formation of baroclinic instability for $E = 0.1$ and $\text{Ro} = 0.01$. We plot $b_0(x, y, z =$
1000 $0) - Bx$ as a function of cross-front coordinate x and along-front coordinate y 72

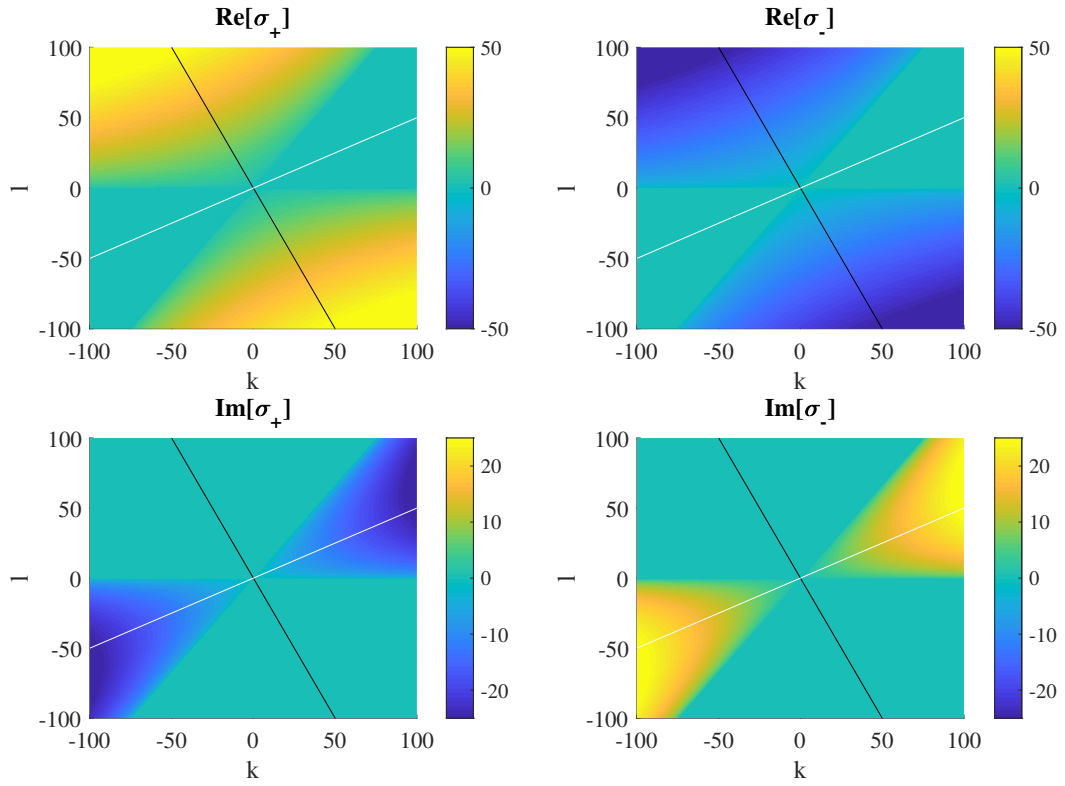


FIG. 1: Real and imaginary parts of the growth rate σ_{\pm} , predicted from the theory for $\mathcal{E} = \mathcal{D} = 0$ and $\mathcal{B}^2 = 0.213$ corresponding to $\alpha = 0.5$ and $B = 2$. The black lines are $k = -\alpha l$ and the white lines are $l = \alpha k$. Note that the top and bottom rows have different color bars.

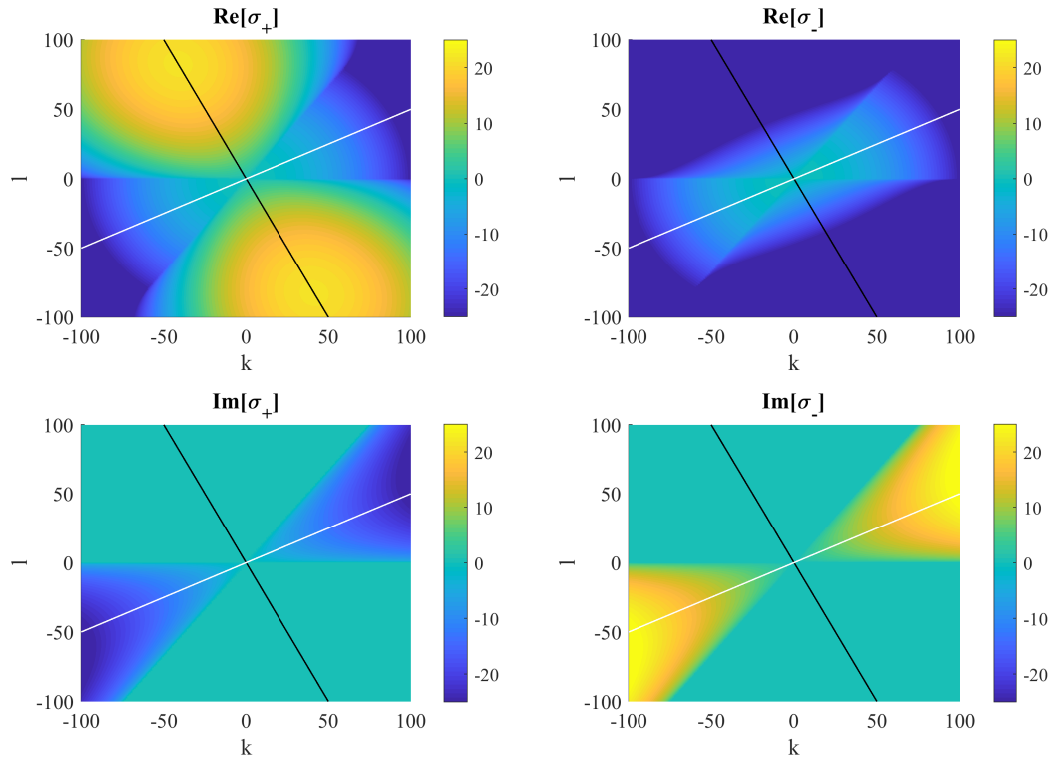


FIG. 2: The real and imaginary parts of the growth rate, σ_{\pm} , predicted from the theory for $\mathcal{E} = \mathcal{D} = 2.5 \times 10^{-3}$ and $\mathcal{B}^2 = 0.213$ corresponding to $\alpha = 0.5$ and $B = 2$. The black lines are $k = -\alpha l$ and the white lines are $l = \alpha k$.

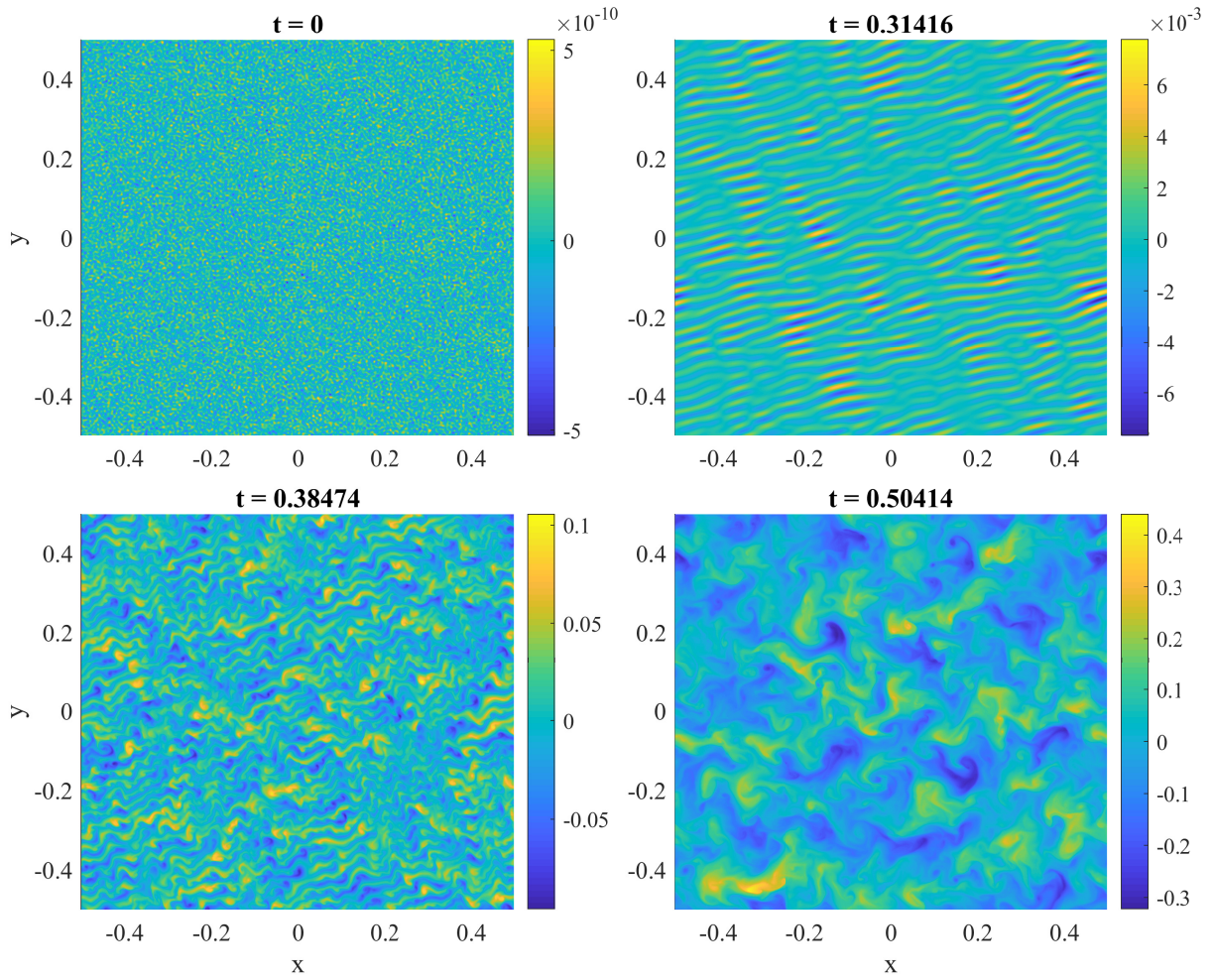


FIG. 3: Depth-averaged buoyancy perturbation, $\bar{b}(x, y) - Bx$ from a nonlinear numerical simulation with $\text{Ro} = 10^{-3}$ and $\alpha = 0.4$ at several times as indicated. The formation of the linear instability and the transition to nonlinear instability can be seen.

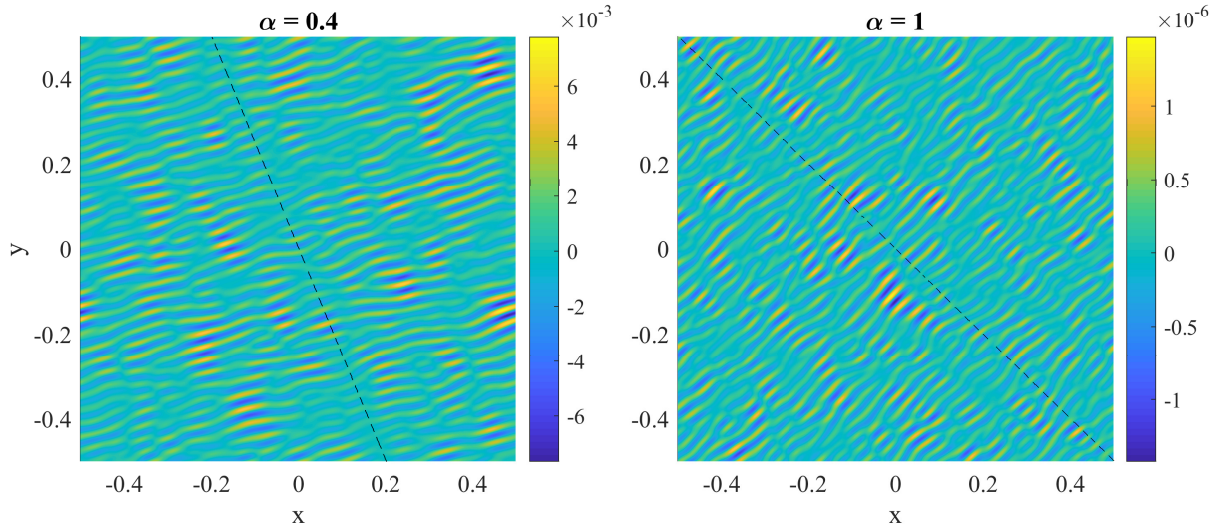


FIG. 4: Depth-averaged buoyancy perturbation, $\bar{b}(x,y) - Bx$ from numerical simulations with $\alpha = 0.4$ and $\alpha = 1$. In both cases $\text{Ro} = 10^{-3}$ and the fields are shown at time $t = 0.314$. The black lines show the predicted wavevector direction, $k = -\alpha l$, which should be perpendicular to lines of constant phase.

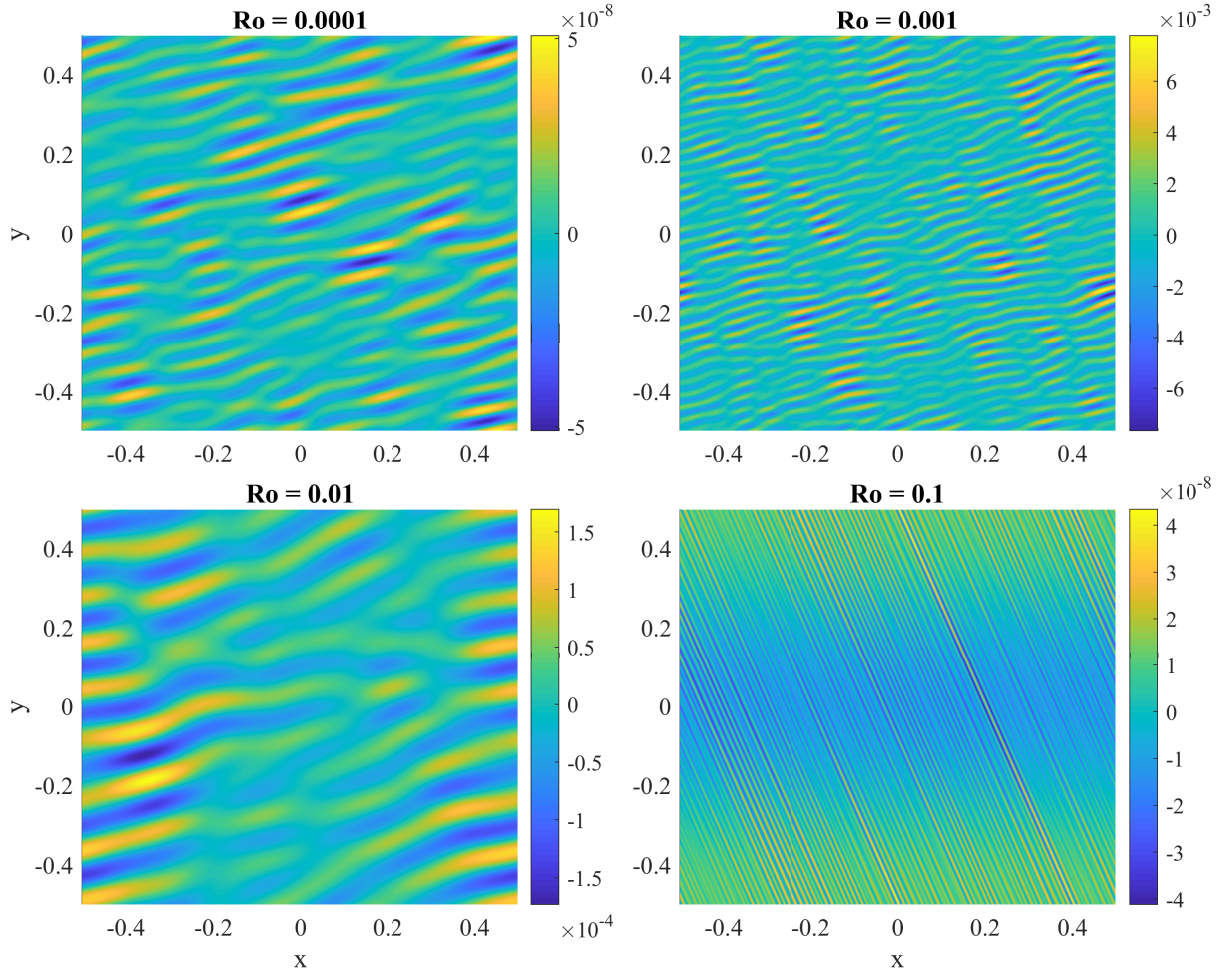


FIG. 5: Depth-averaged buoyancy perturbation, $\bar{b}(x, y) - Bx$ for $\alpha = 0.4$ and several Rossby numbers during the phase of linear perturbation growth in several numerical simulations. For $\text{Ro} = 0.1$ growing modes appear which are perpendicular to those predicted by the analytical theory, indicating a breakdown of the theory due to the relatively large Rossby number.

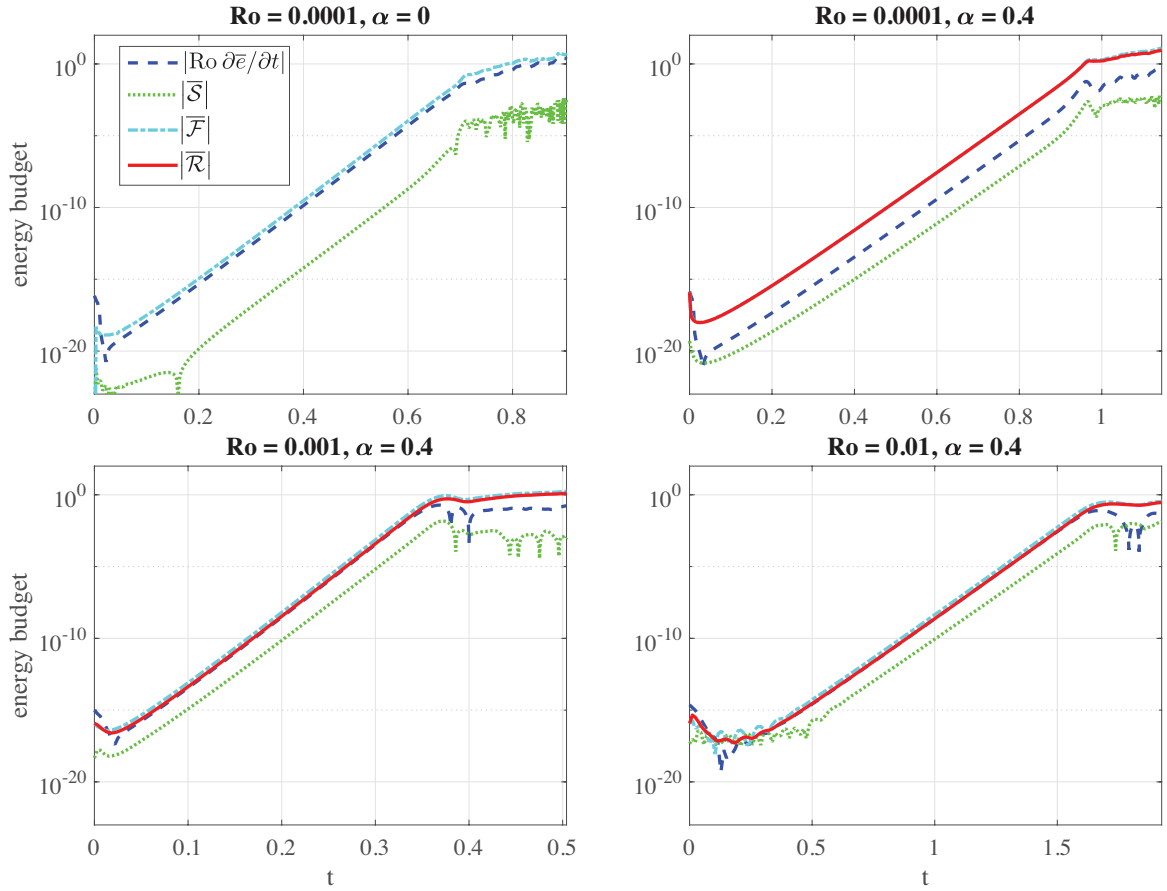


FIG. 6: The magnitude of terms in the volume-averaged energy budget from numerical simulations for several values of Rossby numbers and α . The terms are as given in Eqs. 77 and 78, specifically, the shear production is denoted \bar{S} , buoyancy flux, \bar{F} , and dissipation via vertical mixing (relaxation), \bar{R} . The case of $\alpha = 0$ corresponds to the classical Eady model.

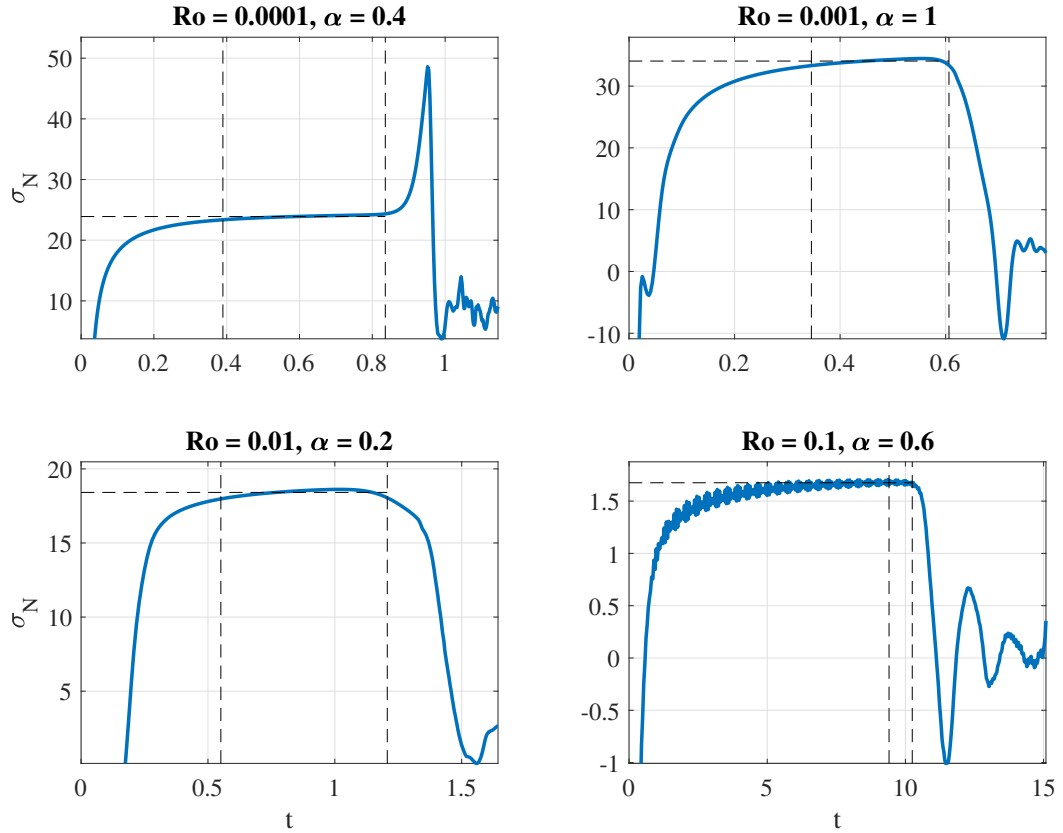


FIG. 7: Perturbation growth rate, σ_N , diagnosed from the numerical simulations for a range of Rossby numbers, Ro and relaxation ratios, α . The dashed lines show the interval of exponential growth and the average value of σ_N within this region.

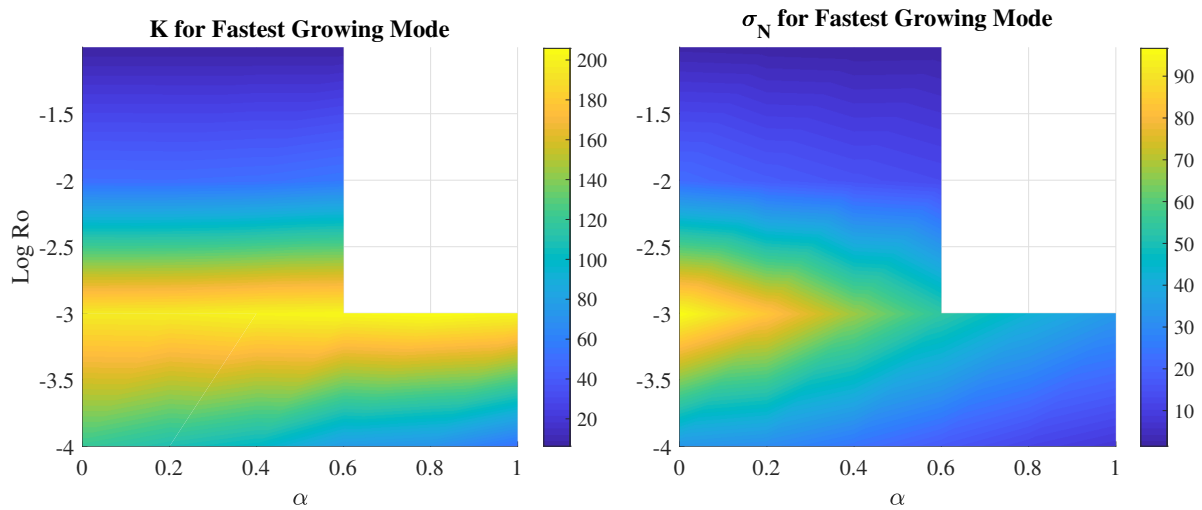


FIG. 8: Perturbation growth rate, σ_N , and the wavenumber, $K = \sqrt{k^2 + l^2}$, for the fastest growing mode inferred from the numerical simulations as functions of Ro and α .

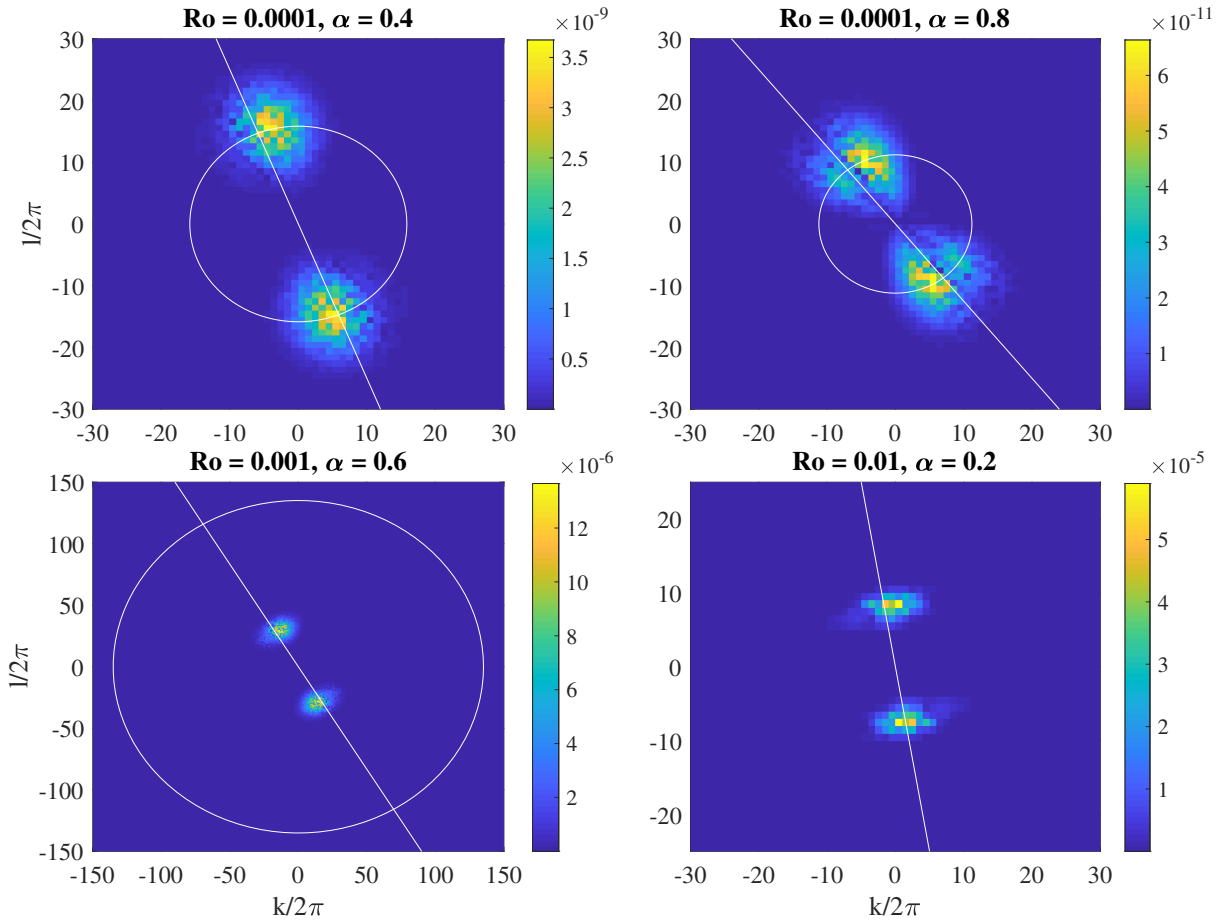


FIG. 9: Amplitudes of the horizontal Fourier coefficients from the depth-averaged buoyancy perturbation, $\bar{b}(x,y) - Bx$, calculated from the numerical simulations for a range of Ro and α . The line $k = -\alpha l$ is shown in white and the maximum wavenumber, K_{max} , is given by the white circle.

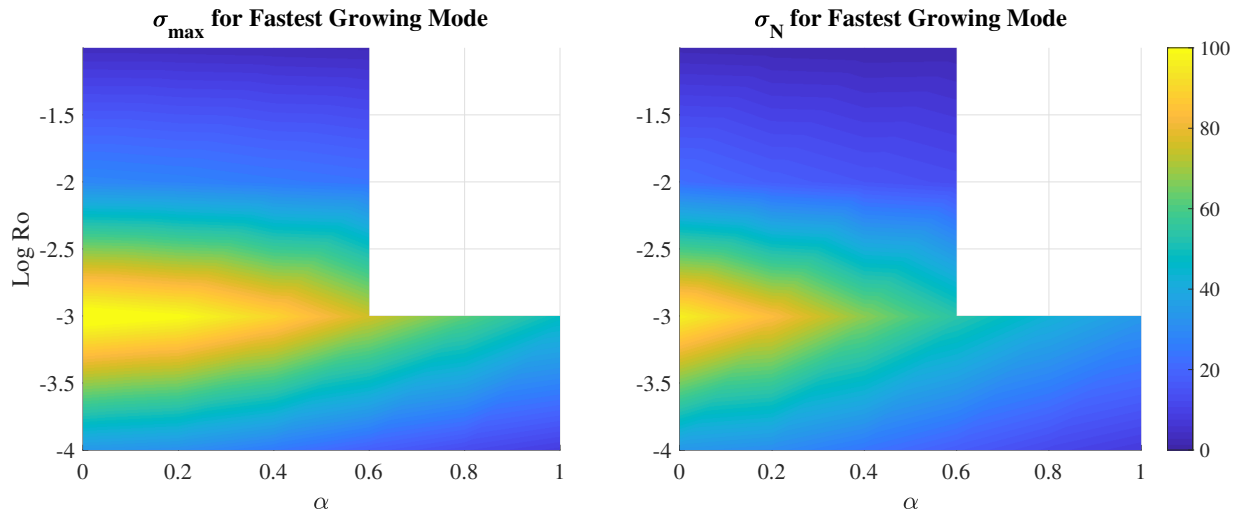


FIG. 10: Perturbation growth rate, σ , diagnosed from the numerical simulations (σ_N) and the maximum growth rate predicted from the theory (σ_{max}).

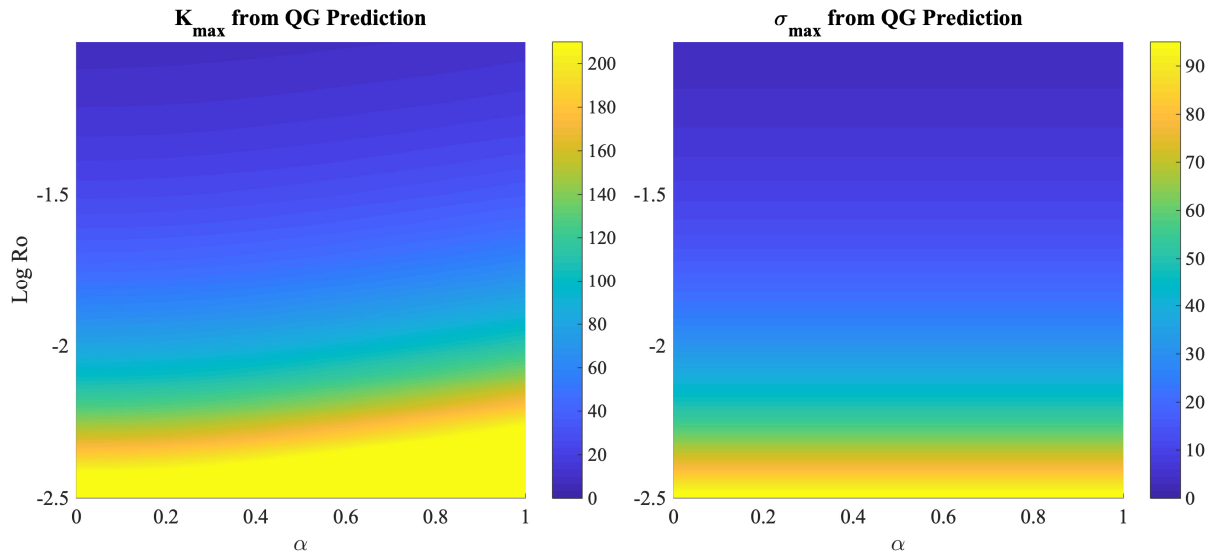


FIG. 11: Wavenumber and growth rate of the most unstable mode from the QG analysis (Eqs. 94 and 95) as functions of Ro and α .

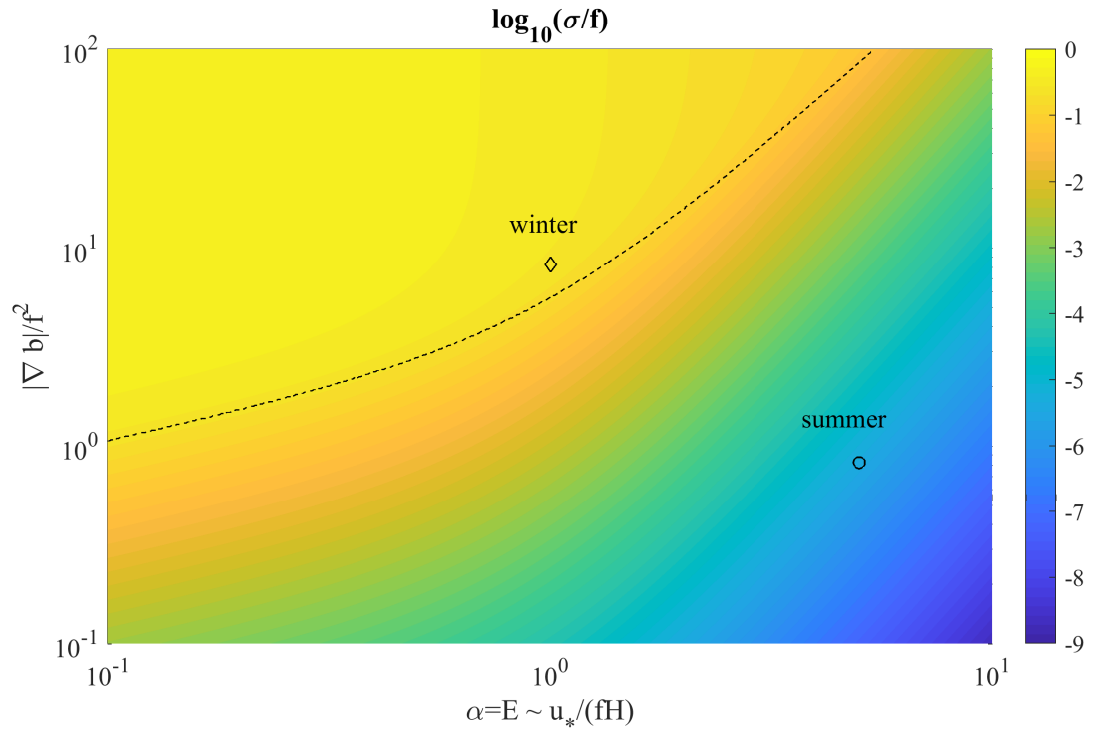


FIG. 12: Predicted growth rate of the most unstable modes from Eq. 102 where the wavenumber is set by the smaller of Eq. 103 and 104. The dashed line separates regions where the wavenumber is set by Eq. 103 (below the line) from regions where the wavenumber is set by Eq. 104 (above the line). The symbols indicate typical parameters from the OSMOSIS survey as reported in Thompson et al. (2016) in the winter and summer (see Table 2 for values).

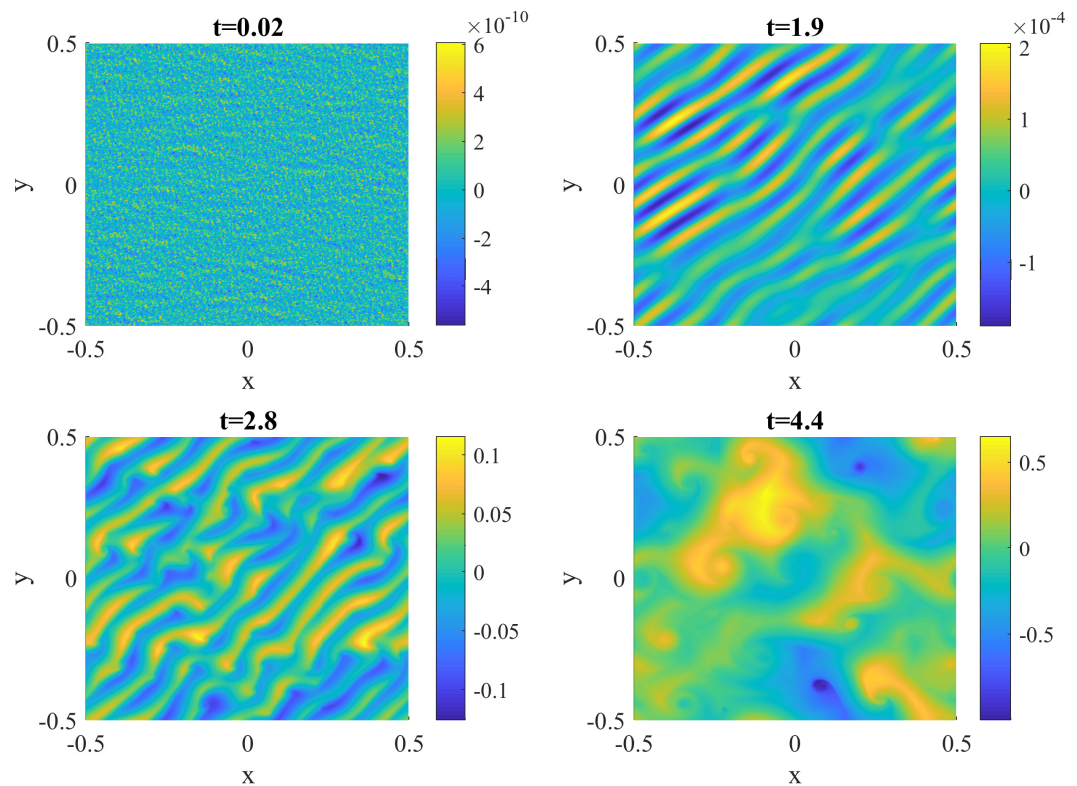


Fig. C1: The formation of baroclinic instability for $E = 0.1$ and $Ro = 0.01$. We plot $b_0(x, y, z = 0) - Bx$ as a function of cross-front coordinate x and along-front coordinate y .